JOURNAL OF GEOPHYSICAL RESEARCH, VOL. 99, NO. B12, PAGES 23,951–23,974, DECEMBER 10, 1994

Present-day crustal deformation in southern California

Hadley O. Johnson, Duncan Carr Agnew, and Frank K. Wyatt

Institute of Geophysics and Planetary Physics, Scripps Institution of Oceanography
University of California, San Diego

Abstract. The effects of laterally homogeneous mantle electrical conductivity have been included in steady. Using an extensive set of precise geodetic measurements, we have developed a detailed picture of present-day deformation rates in southern California. This large set of measurements, amounting to nearly 2000 repeated distance measurements over the period 1973 to 1991, comes from the U.S. Geological Survey's Geodolite trilateration program, involving their combined Anza, Joshua Tree, and Salton networks. Building on previous results from these data, we are able to present the deformation field as estimates of the rate of horizontal strain accumulation in small four-station subnetworks of the overall 89-station network. Using this technique, the spatial details of the 18-year average strain rate field can be determined. By correlating these spatial details with the tectonics of the region we are able to understand better how deformation is partitioned across this highly complex margin between the Pacific and North American tectonic plates. Some of the more interesting findings of this study are that (1) the vast majority of strain rate estimates show a pattern of nearly pure shear as would be expected in a transcurrent environment, (2) the fastest accumulation of surface strain in southern California is along the San Jacinto Fault west of the Salton Sea, not along the San Andreas Fault, (3) strain accumulation rate along the length of the San Jacinto Fault increases toward the southeast as the fault enters the Imperial Valley, (4) a large area near the southern end of the Salton Sea, where the San Andreas Fault meets the Brawley Seismic Zone, is undergoing areal dilatation, which is in part consistent with the formation of crust at a spreading center, and (5) deformation at the transition zone between the San Andreas Fault and the Eastern California Shear Zone also appears to be the result of crustal spreading.

Introduction

During the past 20 years the U.S. Geological Survey (USGS) has made thousands of point-to-point distance measurements using Geodolite electronic distance measurement (EDM) equipment along the active margin between the North American and Pacific plates [*Savage,* 1983]. Much of our knowledge about present-day crustal deformation in the western United States comes from this large set of measurements. Numerous studies covering deformation in southern California have used these data, including *Savage et al.* [1979], *Savage et al.* [1981], *King and Savage* [1983], *Savage et al.* [1986], and *Lisowski et al.* [1991]. Lisowski et al., in particular, discuss the crustal velocity field from the Mexican border north to San Francisco along the San Andreas fault system and serves as an excellent overview and starting point for this study.

We have used these trilateration data to determine the spatial details of the interseismic deformation field in southern California (south of the Transverse Ranges) in what the USGS calls the Anza, Joshua Tree, and Salton EDM networks (Figure 1). By dividing these large networks into many smaller subnetworks, we can map out the variability in deformation as it relates to the tectonic features of the region. In particular, we can determine whether crustal strain is generally accumulating directly over the active faults in the region as "block models" of fault mechanics would predict [e.g., *Bilham and Beavan,* 1979; *Nicholson et al.*, 1986], or if it accumulates over more broadly distributed areas, as an elastic dislocation model would predict [e.g., *Savage,* 1983]. Also of interest is simply identifying which of the many parallel faults in southern California are accumulating the majority of the strain and whether the amount of strain accumulation shows any variability along the length of the faults, possibly suggesting preferred locations for future earthquakes.

Lisowski et al. [1991] presented the deformation field as a plot of the velocity of each geodetic station. This technique results in a good visual representation of the deformation field as a whole but makes it rather difficult to understand the local details since the differences between neighboring station velocities must be mentally estimated and visualized. There is also the complication that the velocity field is not uniquely determined from the trilateration data since the Geodolite measurements are not tied to an external reference frame. (*Lisowski et al.* [1991] remove this ambiguity by minimizing the velocity components in each large EDM network in a direction perpendicular to the direction of maximum shear strain rate in that network.) If instead, the deformation field is presented in terms of the strain rate in many small subnetworks, there is no ambiguity to remove (because strain estimates do not require an external reference frame) and spatial details are a natural by-product. Of course, the uncertainty in the strain rate estimates in each subnetwork will depend on the amount of data available, so there is a trade-off in the accuracy of the estimates as the size of the subnetworks (number of stations

Paper number 94JB01902.
0148-0227/94/94JB-01902$05.00

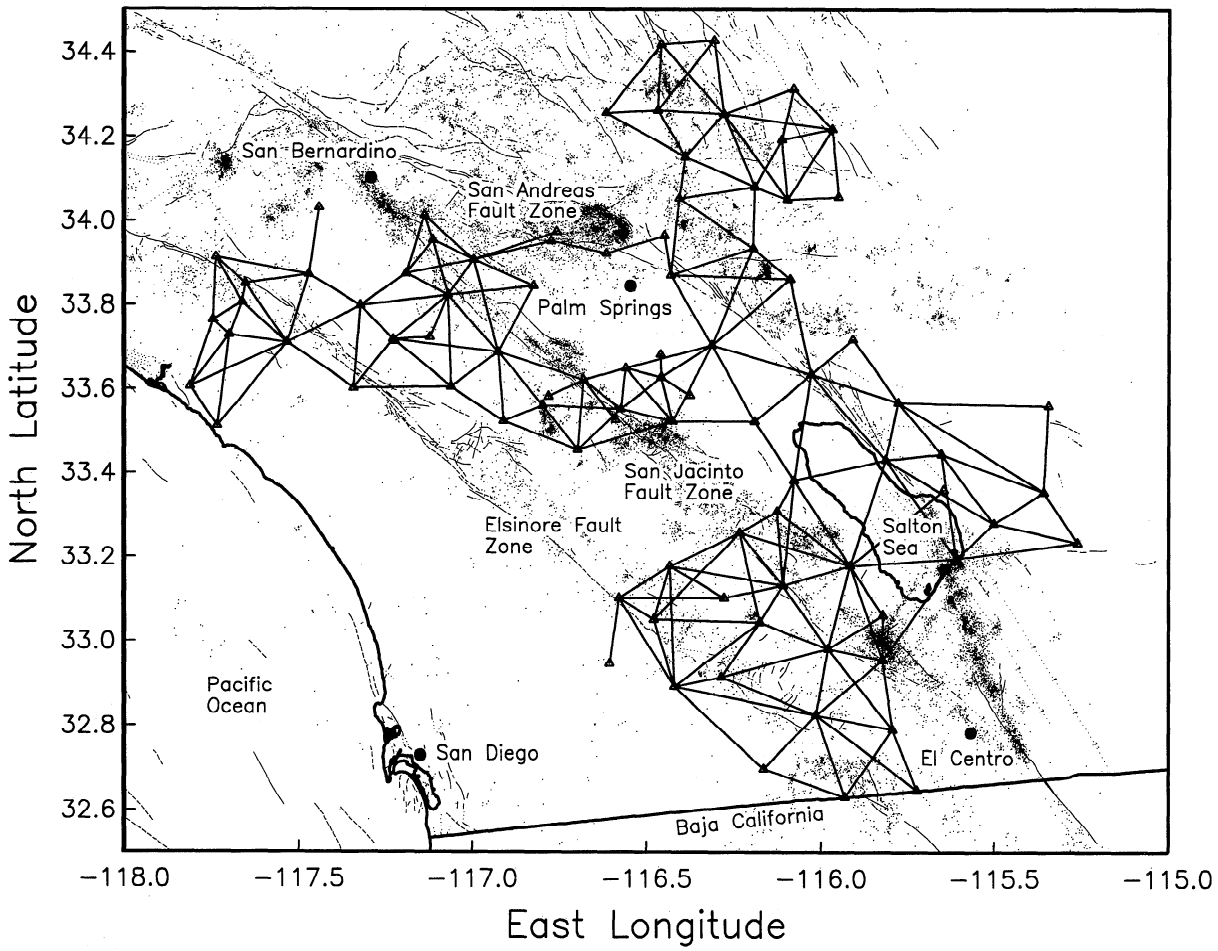

Figure 1. Geodolite network in southern California monitored by the U.S. Geological Survey (USGS) from 1973 to 1991. The seismicity is from the California Institute of Technology/USGS (Caltech/USGS) catalog for the period 1976-1991 ($M_L > 1.5$); fault locations are from the *Jennings* [1988] map of Quaternary faulting. The area west of Palm Springs is called the Anza subnetwork, east of Palm Springs is the Joshua Tree subnetwork, and south of the northern extent of the Salton Sea is the Salton subnetwork.

involved) is reduced. Only because the Geodolite data are of such high, and uniform, quality and span such a long time period is it possible to recover the details of the strain rate field in this manner.

Savage and Prescott [1973] discuss in detail the field techniques used and the measurement accuracy attained by the Geodolite program. Effectively, the point-to-point slope distance between two geodetic markers is determined by measuring the time of flight of a modulated laser beam. To convert this time into a distance, the average index of refraction along the beam path is determined through a combination of end point measurements of atmospheric pressure and temperature and humidity profiles taken along the beam path measured from an aircraft. The slope distance is measured several times over the course of a few hours, and an average value is determined. *Savage et al.* [1986] estimate that the uncertainty in any individual measurement is given by

$$\sigma^2 = a^2 + b^2L^2 = (a_s^2 + a_r^2) + (b_s^2 + b_r^2)L^2, \quad (1)$$

where a is a constant error term, b is a length proportional error term, and L is line length. The random error components (a_r and b_r) have been estimated by *Savage et al.* [1986] to be $a_r = 3$ mm and $b_r = 0.14$ ppm. The systematic error components (a_s and b_s) are largely a result of calibration errors of the meteorological equipment and have been shown to be $a_s = 0.5$ mm and $b_s = 0.14$ ppm. Taken together, these result in an overall estimated error with $a = 3$ mm and $b = 0.2$ ppm. As an example, for line lengths of 5 and 40 km this results in estimated errors of ±3 and ±9 mm, respectively. These errors are roughly comparable with estimates of the accuracy of the Global Positioning System (GPS) when used in the relative positioning mode over these distances [*Davis et al.*, 1989; *Happer et al.*, 1991].

Method

Several techniques are available to estimate the horizontal strain rate tensor from geodetic measurements. Broadly speaking there are two ways in which to proceed and a

third which combines aspects of each: (1) we could use a method that relies on estimating the actual coordinates of each of the geodetic stations as a function of time and then estimate the strain rate tensor by differencing these coordinates, or (2) we could use a method that estimates the strain rate tensor directly from the geodetic measurements by using the survey-to-survey change only for those measurements which are exactly repeated at each survey. There are advantages to each style of analysis. The second method is easier to implement because there is no intermediate step of estimating coordinates before the strain rate tensor is found, but it works only in cases where the same type of measurement (point-to-point distance, vector distance, angle, etc.) is repeated between sets of geodetic stations for each survey and where the amount of time required to fully survey a network is small compared to the rate at which deformation is taking place (so that each survey can be considered to have occurred at a single point in time) [*Frank,* 1966]. On the other hand, the first method is able to use mixed sets of measurements, whether the same type of measurement is made between sets of stations at each epoch or not, and does not require that the same sets of stations be occupied for each survey, nor does it require that resurveys be carried out all at once [*Margrave and Nyland,* 1980; *Brunner et al.,* 1981]. Unfortunately, this flexibility comes at a price, in that the coordinates of the geodetic stations cannot be fully determined from the measurements taken in a typical survey because they are usually not tied to a rigid reference frame (future GPS measurements should be able to get around this problem). The reference frame ambiguity can be overcome by a careful use of the "inner coordinate" solution for each survey [*Brunner et al.,* 1981], but this then reintroduces the requirement that surveys be done all at once, which is not always possible, especially with large networks.

The third method for determining the strain rate tensor from geodetic measurements simultaneously determines the coordinates of the stations and the strain rate tensor which best fits the time change of those coordinates [*Bibby,* 1973, 1975; *Snay and Cline,* 1980; *Bibby,* 1981, 1982]. By combining the coordinate and strain rate tensor estimations into a single procedure, *Bibby* [1982] shows that we retain the

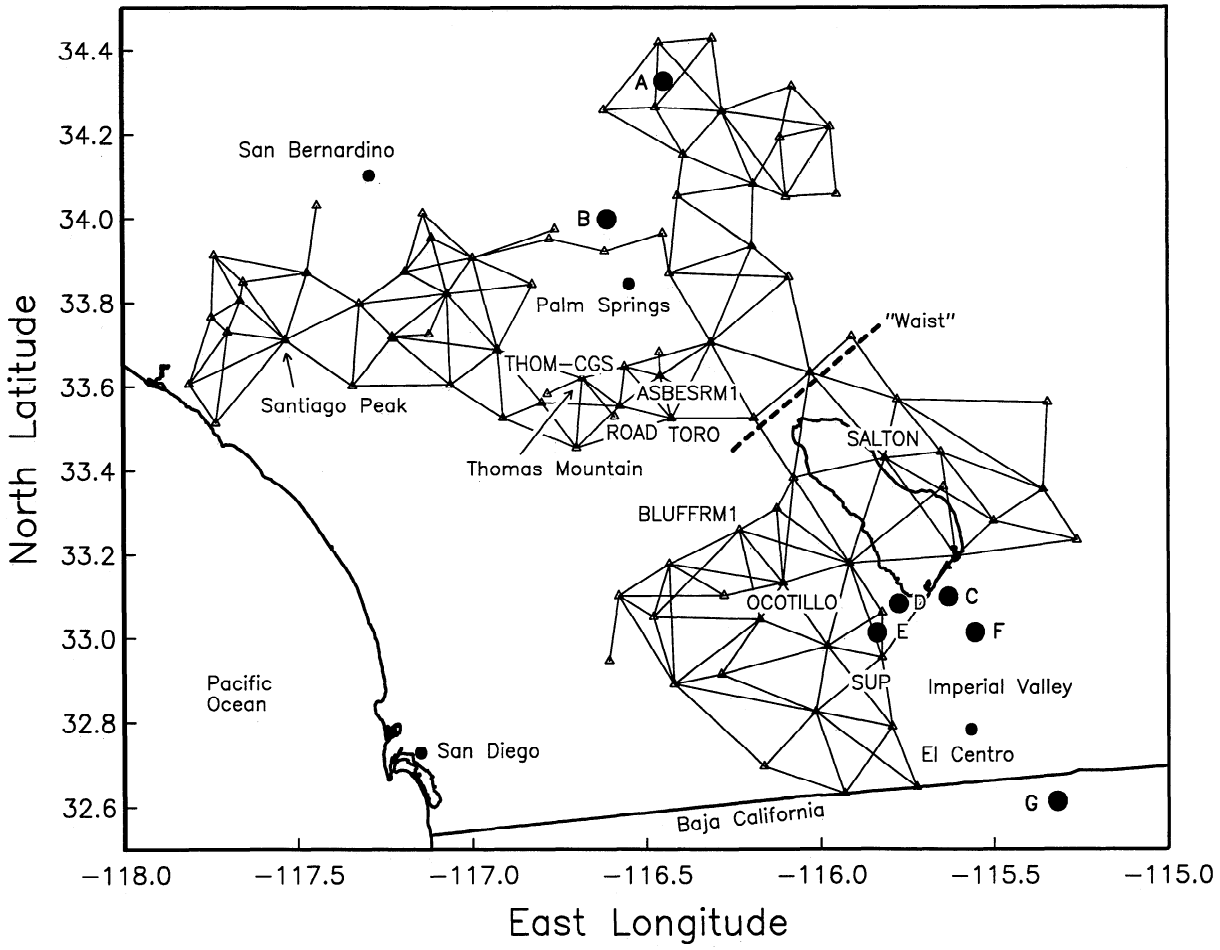

Figure 2. Location of individual Geodolite stations and geographic locations referred to in the text. The seven earthquakes which caused measurable coseismic offsets (labeled A through G from north to south) are Homestead Valley (1979, M_L 5.2), North Palm Springs (1986, M_L 5.6), Westmorland (1981, M_L 5.7), Elmore Ranch (1987, M_L 5.9), Superstition Hills (1987, M_L 6.1), Brawley (1979, M_L 5.9), and Imperial Valley (1979, M_L 6.6).

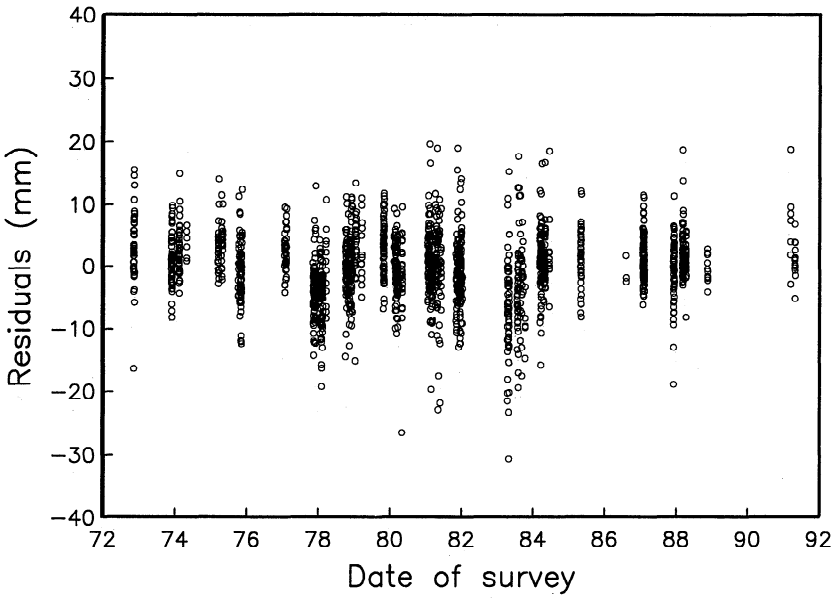

Figure 3. Residuals from a best linear fit to each individual Geodolite line. The yearly surveys tend to bunch together as a group either above or below zero depending on the systematic errors due to slight miscalibrations of the meteorological equipment used to estimate the index of refraction of the atmosphere at the time of the measurements.

advantages of dealing with mixed data types and non repeated surveys, while at the same time not incurring the reference frame ambiguity since all data are processed simultaneously instead of one epoch at a time. The result is that the estimates of the strain rate tensor using this simultaneous reduction method are unaffected by the choice of coordinate systems. Intuitively, this makes sense; the strain rate tensor should only depend on changes in the measured geodetic quantities and not on the particular reference frame used to describe them.

For the USGS Geodolite data, the networks are normally resurveyed in exactly the same way from year to year and there is no difference between the simultaneous reduction method and the method of *Frank* [1966] discussed above, which is used by the USGS in their analyses (see also *Prescott* [1976]). We have chosen to implement the

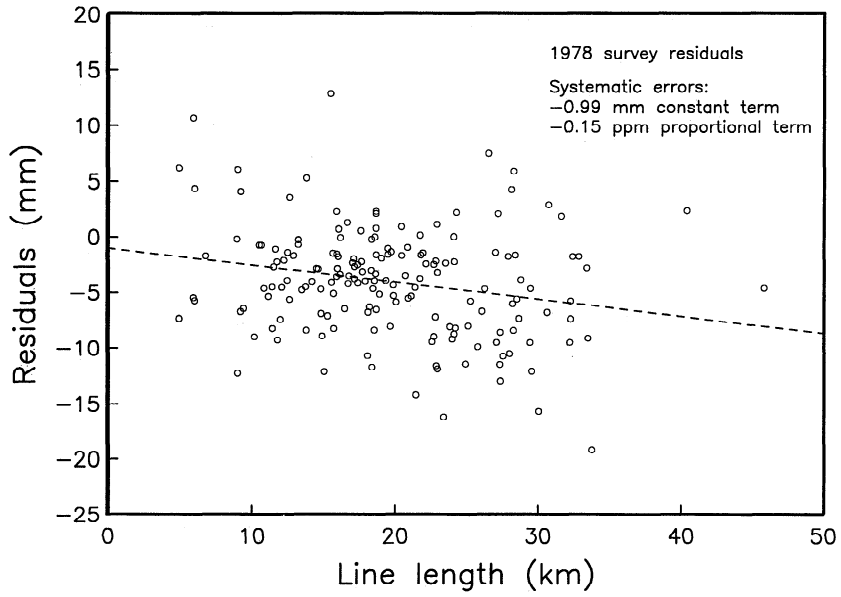

Figure 4. Residuals from a best linear fit for all measurements made between 1977.5 and 1978.5. The least squares trend through the data gives an estimate of the constant and length-dependent systematic errors during this particular campaign.

Table 1. Systematic Errors in Yearly Surveys

Dates Included		Constant Offset,	Length Dependent,
Start	End	mm	ppm
1972.0	1973.0	-3.8	0.31
1973.5	1974.5	3.5	-0.08
1975.0	1975.5	-1.0	0.24
1975.5	1976.0	2.6	-0.17
1977.0	1977.5	2.3	0.01
1977.5	1978.5	-1.0	-0.15
1978.5	1979.5	-0.7	0.05
1979.5	1980.0	1.0	0.08
1980.0	1980.5	1.6	-0.13
1981.0	1981.5	-1.0	0.06
1981.5	1982.5	-2.5	0.08
1983.0	1984.0	0.0	-0.23
1984.0	1984.5	1.3	-0.00
1985.0	1985.5	0.2	0.08
1986.5	1987.5	-0.9	0.11
1987.5	1988.0	0.6	-0.03
1988.0	1988.5	1.1	0.05
1988.5	1989.0	0.6	-0.05
1991.0	1991.5	-1.5	0.27

simultaneous reduction method for this study simply to have it available for future projects.

Whatever method is used to estimate the strain rate tensor from the geodetic measurements, two important assumptions come into play. First, all techniques assume that the deformation taking place within the network, or subnetwork, is spatially uniform. As the size of a subnetwork becomes smaller, this approximation becomes better, but even when the smallest possible strain-rate-determining subnetwork of three Geodolite stations is considered, the spatial extent is still of the order of 10 km because of the interstation spacing involved. Whether the network used is large or small, the methods described here will return the spatially averaged strain rate estimate. The second assumption is that the accumulation of strain is uniform from survey to survey. In this study we use the entire 18-year span of measurements to estimate a single strain rate for each subnetwork and so make an even stronger assumption that this rate was constant over the whole 18-year period. Again, each method considered will return the best average strain rate estimate whether this assumption is valid or not. *Savage et al.* [1986] show that the data used here are consistent with linear strain accumulation, and we use this result in our calculations below.

The best way to satisfy both of these assumptions would be to process the Geodolite data in the smallest possible subnetworks over the shortest possible time spans. However, when the data are broken up in this manner there are not enough measurements to produce robust strain rate estimates. As stated above, we resolve this problem by using the full 18-year span of data to determine a single average strain rate value. Even with this temporal averaging we found when the data are restricted to subnetworks of three stations each (the minimum number to determine all components of the horizontal strain rate tensor), the strain rate estimates have unacceptably large uncertainties. The strain rate uncertainties proved to be significantly smaller for four-station networks, and so all results in this study are for this configuration.

Once the strain rate tensor has been estimated, we require a way to plot this on a map to understand the results. The style we use follows the USGS convention of representing the principal strain rate tensor by four arrows emanating from the center of the subnetwork. As an example, the inset in Figure 7 shows the representations for pure shear (equal and opposite linear strain at 45° to the shear) and positive areal dilatation.

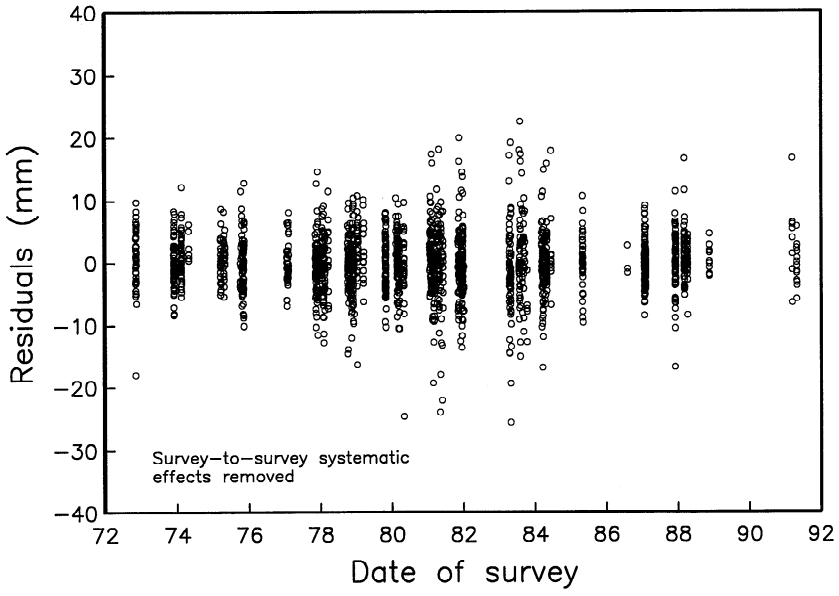

Figure 5. Residuals from a best linear fit to each individual Geodolite line after the year-to-year systematic effects have been removed. The constant and length-dependent systematic error terms for each year are estimated as in Figure 4 and have been removed from the raw Geodolite data.

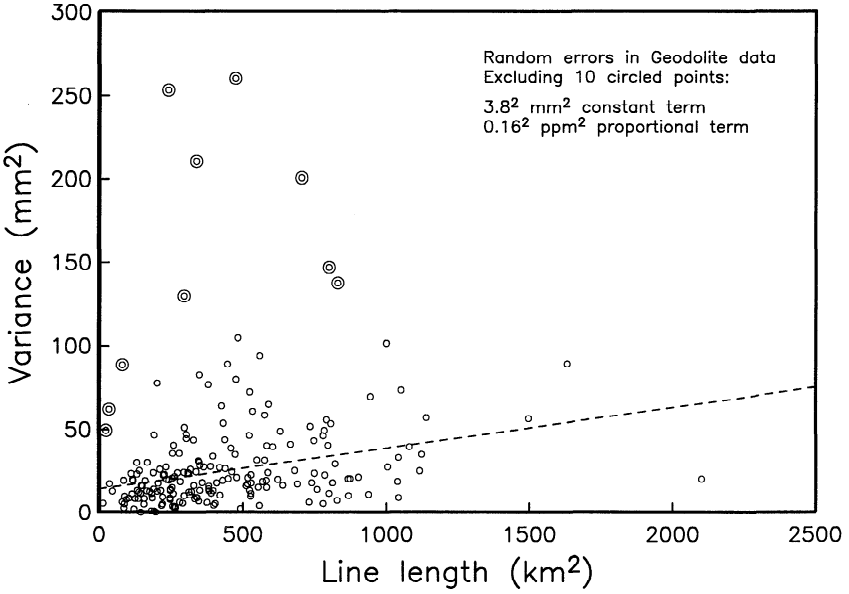

Figure 6. Estimated variance of the residuals from a linear fit for each individual Geodolite line in the network after the systematic effects have been removed. The 10 circled points correspond to lines which have abnormally large residuals during the early 1980s when the USGS subcontracted the field work to private surveying companies. They were temporarily removed before the data were fit for the constant and length-dependent random error terms.

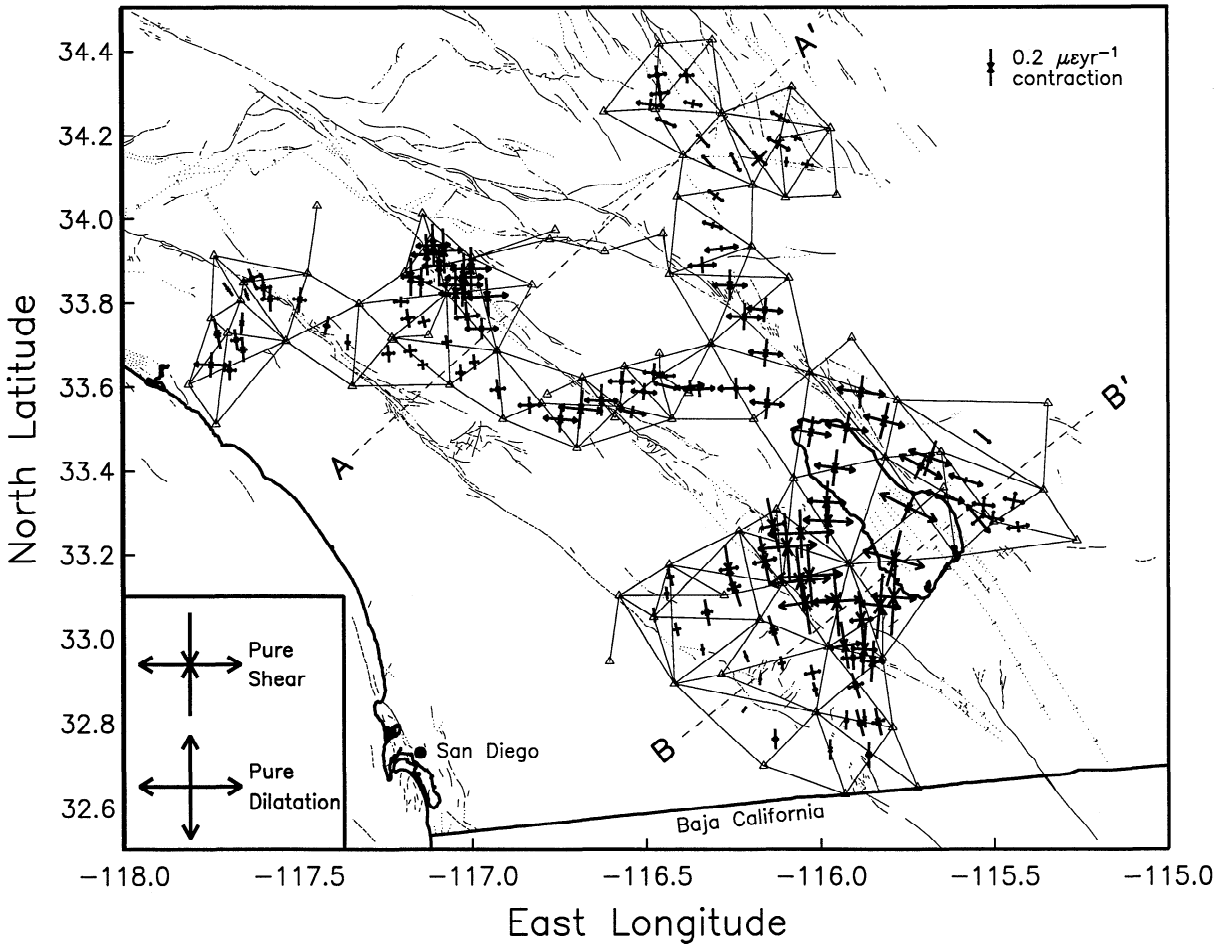

Figure 7. Principal horizontal strain rates for all combinations of four neighboring Geodolite stations plotted at the centers of the four-station subnetworks. The inset in the lower left depicts the plotting conventions used.

Geodolite Data

Organization of Data

The following section describes the steps taken before using the Geodolite data to calculate the horizontal strain rate tensors. We discuss our handling of the earthquakes which occurred during the 18-year span of measurements, steps taken to deal with "defects" in the geometry of some of the subnetworks used, and other details. In addition, we analyze the data as a whole to produce independent esti-

Table 2. Four-Station Subnetwork Principal Strain Rate Estimates

Stations in Subnetwork[1]				long.[2]	lat.[2]	$\dot{e}_1$[3]	$\sigma_{\dot{e}_1}$	α_1[4]	σ_{α_1}	$\dot{e}_2$	$\sigma_{\dot{e}_2}$	α_2	σ_{α_2}
carrizo	dixie	off_225	off_229	-115.86	32.72	0.035	0.010	90.1	3.1	-0.138	0.012	0.1	3.1
carrizo	dixie	off_229	jacumba	-115.97	32.74	0.001	0.010	89.2	4.4	-0.111	0.012	-0.8	4.4
carrizo	off_229	jacumba	monu_res	-116.13	32.76	0.034	0.013	88.3	3.7	-0.108	0.013	-1.7	3.7
carrizo	jacumba	monu_res	stage	-116.22	32.83	0.004	0.019	125.1	25.8	-0.037	0.026	35.1	25.8
carrizo	monu_res	stage	fish	-116.17	32.90	0.015	0.012	93.4	13.2	-0.060	0.018	3.4	13.2
fish	carrizo	stage	elephant	-116.11	32.94	0.037	0.014	79.6	8.0	-0.075	0.018	-10.4	8.0
fish	stage	monu_res	elephant	-116.21	32.96	0.013	0.022	69.0	18.2	-0.066	0.048	-21.0	18.2
stage	fish	dixie	carrizo	-116.02	32.88	0.021	0.012	74.5	7.3	-0.077	0.016	-15.5	7.3
stage	fish	sup	carrizo	-116.02	32.92	0.084	0.011	77.7	4.1	-0.082	0.018	-12.3	4.1
fish	sup	dixie	carrizo	-115.90	32.89	0.085	0.011	71.8	2.4	-0.139	0.012	-18.2	2.4
fish	dixie	off_225	carrizo	-115.88	32.81	0.002	0.016	84.4	8.7	-0.092	0.014	-5.6	8.7
fish	dixie	off_229	carrizo	-115.93	32.81	-0.029	0.013	93.4	8.7	-0.098	0.010	3.4	8.7
sup	dixie	off_229	carrizo	-115.89	32.80	0.028	0.012	74.3	3.1	-0.138	0.011	-15.7	3.1
sup	dixie	off_225	carrizo	-115.84	32.80	0.067	0.011	76.2	2.4	-0.144	0.013	-13.8	2.4
soda	kane	sup	fish	-115.88	33.04	0.121	0.015	84.5	1.4	-0.307	0.010	-5.5	1.4
soda	sup	dixie	fish	-115.88	32.98	0.137	0.021	93.4	2.0	-0.269	0.010	3.4	2.0
soda	sup	carrizo	fish	-115.93	32.98	0.170	0.016	80.5	1.5	-0.247	0.010	-9.5	1.5
kane	sup	dixie	fish	-115.85	32.95	0.132	0.015	93.5	2.1	-0.222	0.014	3.5	2.1
kane	sup	carrizo	fish	-115.91	32.95	0.126	0.016	86.7	3.5	-0.128	0.016	-3.3	3.5
elephant	stage	monu_res	granite	-116.34	32.98	0.017	0.018	81.2	12.9	-0.062	0.021	-8.8	12.9
stage	fish	ocotillo	elephant	-116.14	33.02	0.048	0.018	70.6	3.7	-0.160	0.022	-19.4	3.7
elephant	fish	soda	ocotillo	-116.04	33.08	0.287	0.015	81.6	1.1	-0.328	0.013	-8.4	1.1
monu_res	wilson	volcan	granite	-116.48	33.06	0.004	0.022	83.3	8.9	-0.075	0.013	-6.7	8.9
volcan	granite	bluffrm1	wilson	-116.43	33.15	0.037	0.021	73.3	7.1	-0.094	0.029	-16.7	7.1
wilson	yak	ocotillo	bluffrm1	-116.26	33.17	0.101	0.014	80.5	3.1	-0.252	0.048	-9.5	3.1
monu_res	granite	bluffrm1	elephant	-116.33	33.06	0.059	0.021	79.6	4.7	-0.134	0.017	-10.4	4.7
granite	elephant	ocotillo	bluffrm1	-116.25	33.12	0.074	0.019	71.0	2.8	-0.210	0.019	-19.0	2.8
volcan	wilson	yak	granite	-116.44	33.11	0.022	0.012	85.1	9.4	-0.069	0.027	-4.9	9.4
elephant	ocotillo	palm	bluffrm1	-116.16	33.19	0.127	0.036	78.3	2.7	-0.265	0.019	-11.7	2.7
ocotillo	bluffrm1	palm	coolidge	-116.14	33.27	0.142	0.034	77.3	2.3	-0.289	0.013	-12.7	2.3
bluffrm1	palm	soda	ocotillo	-116.09	33.22	0.309	0.013	85.5	1.2	-0.356	0.022	-4.5	1.2
palm	coolidge	soda	ocotillo	-116.06	33.25	0.346	0.015	87.3	1.0	-0.256	0.010	-2.7	1.0
palm	soda	fish	ocotillo	-116.03	33.15	0.345	0.015	86.0	0.9	-0.335	0.012	-4.0	0.9
ocotillo	soda	kane	fish	-115.96	33.09	0.260	0.015	85.8	0.9	-0.361	0.013	-4.2	0.9
ocotillo	soda	salton	coolidge	-115.98	33.28	0.260	0.011	92.0	1.2	-0.241	0.009	2.0	1.2
palm	coolidge	salton	soda	-115.98	33.33	0.201	0.012	93.0	1.3	-0.223	0.012	3.0	1.3
soda	sup	alamo	salton	-115.79	33.19	0.334	0.012	104.0	0.7	-0.302	0.009	14.0	0.7
soda	alamo	coach	salton	-115.75	33.31	0.332	0.012	114.9	1.0	-0.166	0.011	24.9	1.0
salton	coach	oldbeach	alamo	-115.64	33.34	0.216	0.012	104.8	3.0	0.039	0.012	14.8	3.0
salton	coach	beals	oldbeach	-115.58	33.38	0.187	0.012	106.5	4.2	0.023	0.026	16.5	4.2
coach	beals	oldbeach	alamo	-115.53	33.32	0.121	0.015	95.1	11.6	0.074	0.013	5.1	11.6
beals	salva	alamo	oldbeach	-115.43	33.27	0.118	0.010	80.5	10.9	0.054	0.029	-9.5	10.9
coach	beals	salva	oldbeach	-115.44	33.33	0.112	0.012	101.0	27.2	0.087	0.024	11.0	27.2
orocopia	butte	beals	coach	-115.53	33.48	0.111	0.024	127.4	7.3	0.006	0.024	37.4	7.3
salton	coach	orocopia	mecca	-115.82	33.52	0.220	0.013	103.4	1.6	-0.196	0.015	13.4	1.6
salton	orocopia	cottonwo	mecca	-115.88	33.59	0.258	0.015	96.3	1.3	-0.174	0.014	6.3	1.3
mecca	orocopia	salton	coolidge	-115.92	33.50	0.228	0.010	99.7	1.4	-0.168	0.010	9.7	1.4
mecca	salton	coolidge	martinez	-116.03	33.49	0.212	0.012	98.9	1.4	-0.160	0.011	8.9	1.4
mecca	salton	soda	coolidge	-115.96	33.41	0.214	0.012	96.8	1.2	-0.192	0.009	6.8	1.2
orocopia	coach	alamo	salton	-115.71	33.41	0.255	0.017	117.4	1.6	-0.140	0.014	27.4	1.6
orocopia	coach	oldbeach	salton	-115.69	33.43	0.238	0.015	108.7	1.5	-0.197	0.015	18.7	1.5
soda	alamo	sup	fish	-115.83	33.08	0.219	0.011	95.5	1.1	-0.343	0.010	5.5	1.1
coach	oldbeach	salva	alamo	-115.50	33.29	0.123	0.010	100.9	12.2	0.071	0.013	10.9	12.2
salton	oldbeach	salva	alamo	-115.55	33.28	0.191	0.017	139.9	6.6	0.089	0.014	49.9	6.6
volcan	granite	elephant	monu_res	-116.41	33.02	0.038	0.017	76.6	7.7	-0.068	0.021	-13.4	7.7
bluffrm1	soda	fish	ocotillo	-116.06	33.14	0.321	0.014	83.8	0.9	-0.342	0.013	-6.2	0.9
soda	alamo	sup	kane	-115.79	33.10	0.238	0.013	93.4	0.9	-0.396	0.011	3.4	0.9
mecca	coolidge	martinez	laquinta	-116.15	33.56	0.179	0.013	95.7	1.5	-0.167	0.010	5.7	1.5
mecca	martinez	toro	laquinta	-116.24	33.60	0.193	0.010	89.2	1.7	-0.111	0.013	-0.8	1.7
mecca	martinez	laquinta	berdoo	-116.16	33.68	0.181	0.012	95.1	1.4	-0.148	0.012	5.1	1.4
mecca	laquinta	inspncer	berdoo	-116.16	33.78	0.187	0.012	95.0	1.8	-0.128	0.012	5.0	1.8
berdoo	laquinta	edom_2	inspncer	-116.26	33.84	0.183	0.013	90.5	1.7	-0.168	0.016	0.5	1.7
mecca	laquinta	edom_2	berdoo	-116.22	33.77	0.188	0.010	92.4	1.8	-0.139	0.012	2.4	1.8
laquinta	martinez	toro	asbesrm1	-116.35	33.59	0.163	0.014	86.8	2.3	-0.078	0.012	-3.2	2.3
laquinta	martinez	toro	eve	-116.37	33.60	0.146	0.010	83.5	2.4	-0.072	0.013	-6.5	2.4
laquinta	toro	lookout	asbesrm1	-116.48	33.63	0.114	0.014	93.7	4.7	-0.105	0.023	3.7	4.7
laquinta	asbesrm1	lookout	eve	-116.44	33.60	0.122	0.014	103.2	5.1	-0.012	0.017	13.2	5.1

Table 2. (Continued)

Stations in Subnetwork				long.	lat.	$\dot{e}_1$	$\sigma_{\dot{e}_1}$	α_1	σ_{α_1}	$\dot{e}_2$	$\sigma_{\dot{e}_2}$	α_2	σ_{α_2}
laquinta	toro	eve	asbesrm1	-116.44	33.63	0.088	0.011	88.5	4.8	-0.019	0.014	-1.5	4.8
asbesrm1	toro	lookout	eve	-116.50	33.59	0.132	0.013	94.7	2.9	-0.086	0.014	4.7	2.9
asbesrm1	toro	moss	lookout	-116.54	33.54	0.147	0.013	101.3	3.4	-0.065	0.021	11.3	3.4
thom_cgs	eve	asbesrm1	lookout	-116.57	33.61	0.143	0.016	91.3	3.3	-0.112	0.022	1.3	3.3
thom_cgs	eve	lookout	moss	-116.63	33.57	0.179	0.022	91.3	2.8	-0.167	0.014	1.3	2.8
thom_cgs	lookout	moss	jason	-116.69	33.55	0.234	0.015	96.2	1.8	-0.199	0.016	6.2	1.8
lookout	moss	roundtop	jason	-116.75	33.52	0.178	0.013	94.3	2.3	-0.140	0.031	4.3	2.3
moss	roundtop	pollycgs	jason	-116.83	33.56	0.121	0.019	89.0	4.6	-0.094	0.019	-1.0	4.6
pollycgs	jason	roundtop	bachelor	-116.92	33.59	0.080	0.019	83.5	3.9	-0.105	0.019	-6.5	3.9
pollycgs	roundtop	bachelor	menifee	-117.03	33.63	0.049	0.014	87.5	5.4	-0.094	0.018	-2.5	5.4
pollycgs	roundtop	bachelor	nelson	-116.99	33.66	0.049	0.021	84.5	5.7	-0.082	0.013	-5.5	5.7
pollycgs	bachelor	menifee	nelson	-117.07	33.71	0.051	0.013	82.4	4.9	-0.067	0.015	-7.6	4.9
pollycgs	bachelor	elsinore	menifee	-117.14	33.65	0.049	0.012	85.1	7.1	-0.055	0.032	-4.9	7.1
pollycgs	bachelor	nelson	ranger	-116.97	33.74	0.175	0.015	89.9	2.4	-0.112	0.013	-0.1	2.4
pollycgs	menifee	nelson	ranger	-117.01	33.77	0.134	0.012	83.2	2.4	-0.148	0.020	-6.8	2.4
pollycgs	menifee	ida	nelson	-117.14	33.76	0.060	0.014	76.6	6.7	-0.063	0.031	-13.4	6.7
pollycgs	nelson	david	ranger	-116.95	33.82	0.219	0.014	86.4	1.6	-0.203	0.014	-3.6	1.6
pollycgs	nelson	gander	david	-117.03	33.84	0.217	0.036	90.1	2.5	-0.230	0.017	0.1	2.5
pollycgs	nelson	micro	david	-117.04	33.82	0.174	0.019	89.9	2.3	-0.220	0.020	-0.1	2.3
ranger	nelson	micro	david	-117.02	33.86	0.203	0.013	88.2	2.2	-0.256	0.048	-1.8	2.2
ranger	nelson	gander	david	-117.00	33.88	0.216	0.014	89.7	2.4	-0.227	0.022	-0.3	2.4
david	nelson	micro	gander	-117.09	33.89	0.178	0.018	90.0	2.1	-0.222	0.020	0.0	2.1
david	micro	brink_2	gander	-117.11	33.94	0.180	0.020	88.2	2.1	-0.223	0.020	-1.8	2.1
nelson	gander	brink_2	david	-117.08	33.92	0.204	0.036	88.2	2.7	-0.236	0.021	-1.8	2.7
nelson	micro	brink_2	gander	-117.13	33.92	0.162	0.033	87.8	2.6	-0.217	0.016	-2.2	2.6
david	nelson	ida	micro	-117.14	33.85	0.116	0.014	92.2	4.1	-0.155	0.050	2.2	4.1
gander	nelson	ida	micro	-117.17	33.86	0.100	0.016	90.3	3.0	-0.200	0.021	0.3	3.0
micro	nelson	menifee	ida	-117.20	33.80	0.080	0.018	92.3	6.5	-0.056	0.054	2.3	6.5
nelson	double	menifee	ida	-117.18	33.76	0.073	0.021	81.8	8.4	-0.098	0.055	-8.2	8.4
bachelor	elsinore	menifee	nelson	-117.17	33.69	0.066	0.015	83.3	5.2	-0.068	0.015	-6.7	5.2
bachelor	elsinore	ida	menifee	-117.24	33.68	0.069	0.016	85.3	5.2	-0.090	0.017	-4.7	5.2
menifee	elsinore	santiago	ida	-117.36	33.71	0.026	0.019	90.4	7.0	-0.080	0.018	0.4	7.0
ida	elsinore	santiago	arling	-117.42	33.75	0.034	0.018	101.7	5.6	-0.101	0.016	11.7	5.6
ida	santiago	sier	arling	-117.49	33.81	0.070	0.016	96.3	3.7	-0.129	0.020	6.3	3.7
arling	santiago	sier	san_juan	-117.60	33.84	0.083	0.015	85.2	4.3	-0.132	0.019	-4.8	4.3
arling	santiago	black	sier	-117.58	33.81	0.095	0.022	88.4	4.3	-0.126	0.019	-1.6	4.3
arling	sier	black	san_juan	-117.63	33.86	0.111	0.026	70.4	8.2	-0.106	0.051	-19.6	8.2
san_juan	sier	santiago	black	-117.64	33.82	0.002	0.141	71.8	67.0	-0.068	0.076	-18.2	67.0
santiago	black	lomas	bee	-117.66	33.75	0.016	0.033	93.6	12.0	-0.113	0.049	3.6	12.0
san_juan	sier	black	lomas	-117.70	33.83	-0.013	0.043	54.1	23.1	-0.085	0.036	-35.9	23.1
black	bee	san_joaq	lomas	-117.73	33.73	0.033	0.066	78.5	12.8	-0.154	0.043	-11.5	12.8
black	santiago	san_joaq	bee	-117.67	33.71	0.055	0.025	82.1	7.3	-0.110	0.041	-7.9	7.3
santiago	bee	san_joaq	niguel	-117.69	33.64	0.069	0.025	91.4	6.7	-0.104	0.024	1.4	6.7
lomas	bee	niguel	san_joaq	-117.75	33.65	0.178	0.081	93.3	4.5	-0.133	0.026	3.3	4.5
black	santiago	niguel	bee	-117.66	33.69	0.042	0.031	86.5	7.4	-0.130	0.026	-3.5	7.4
berdoo	inspncer	warren	edom_2	-116.28	33.93	0.177	0.013	82.5	7.0	0.028	0.023	-7.5	7.0
laquinta	inspncer	warren	edom_2	-116.34	33.89	0.148	0.024	87.1	3.3	-0.085	0.015	-2.9	3.3
inspncer	edom_2	warren	keys	-116.31	33.99	0.109	0.020	105.5	13.0	0.026	0.021	15.5	13.0
inspncer	warren	pax_ncer	keys	-116.30	34.06	0.097	0.030	125.5	7.4	-0.045	0.031	35.5	7.4
warren	keys	sandhill	pax_ncer	-116.32	34.14	0.094	0.027	137.1	9.8	-0.006	0.027	47.1	9.8
keys	sandhill	rich	pax_ncer	-116.33	34.19	0.092	0.029	135.8	12.9	0.005	0.029	45.8	12.9
sandhill	pax_ncer	meeks	rich	-116.44	34.23	0.114	0.028	112.8	10.8	-0.016	0.042	22.8	10.8
sandhill	rich	meeks	maumee	-116.45	34.30	0.103	0.027	83.2	6.5	-0.092	0.029	-6.8	6.5
pax_ncer	rich	maumee	meeks	-116.48	34.27	0.147	0.031	98.2	6.3	-0.060	0.030	8.2	6.3
sandhill	pax_ncer	rich	creolrm2	-116.36	34.28	0.095	0.034	102.0	9.3	-0.044	0.028	12.0	9.3
maumee	creolrm2	sandhill	rich	-116.38	34.34	0.076	0.026	87.4	8.0	-0.080	0.023	-2.6	8.0
creolrm2	rich	meeks	maumee	-116.46	34.34	0.097	0.035	81.6	11.0	-0.107	0.042	-8.4	11.0
sandhill	segundo	valmtecc	mesquite	-116.11	34.24	0.109	0.029	117.5	9.6	-0.037	0.040	27.5	9.6
sandhill	valmtecc	mesquite	queen	-116.11	34.18	0.134	0.022	118.3	4.8	-0.054	0.023	28.3	4.8
mesquite	queen	keys	sandhill	-116.17	34.15	0.104	0.038	135.3	8.2	-0.108	0.038	45.3	8.2
segundo	valmtecc	queen	mesquite	-116.07	34.20	0.055	0.036	110.3	15.1	-0.034	0.027	20.3	15.1
valmtecc	29_palms	queen	mesquite	-116.03	34.13	0.058	0.032	99.5	17.7	-0.046	0.023	9.5	17.7
valmtecc	queen	keys	mesquite	-116.09	34.14	0.018	0.033	94.3	23.7	-0.051	0.028	4.3	23.7
sandhill	queen	keys	pax_ncer	-116.24	34.14	0.108	0.029	152.1	9.3	-0.021	0.030	62.1	9.3

1. Subnetworks presented in approximately south to north ordering. 2. Coordinates of center of subnetwork. 3. Strain rates in microstrain per year with $\dot{e}_1$ the most extensive strain rate. 4. Azimuths in degrees clockwise from north.

mates of the error terms in equation 1. (See *Savage et al.* [1986] for plots of much of the raw line length data.) Readers more interested in the strain rate estimates may wish to skip this section.

Several earthquakes occurred in southern California during the span of the Geodolite program. Since we are interested in only the accumulation of interseismic strain, these earthquakes are "noise" and their effect on the data must be removed. There are two ways to achieve this. One possibility is to model the fault-slip distributions of these earthquakes and to use an elastic dislocation program to calculate the change in length for each of the Geodolite

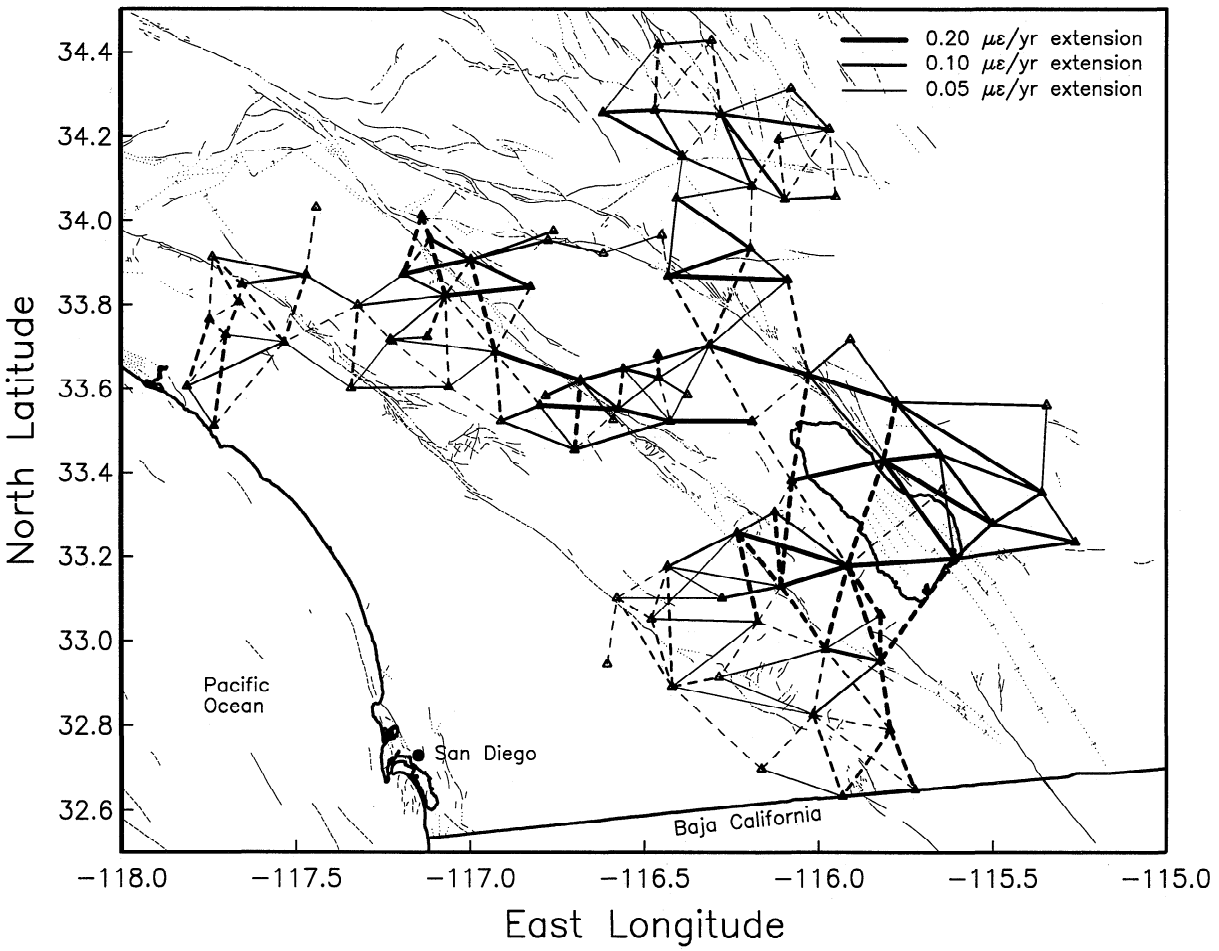

Figure 8. Average linear strain rate for each individual Geodolite line. Solid lines represent extension and dashed lines represent contraction. The thickness of the lines is proportional to the amount of strain rate. Because the southern California area is dominated by northwest-southeast shear, the majority of the Geodolite lines directed approximately north-south show contraction, while the east-west lines show extension.

lines and then to remove these modeled offsets from the data. This procedure often turns out to be a bit circular since in many cases these same Geodolite data have been used by other researchers to estimate the coseismic fault-slip distributions in the first place. Instead, using the assumption that strain accumulates linearly in time as discussed in the previous section, we chose to determine the best fitting offset at the time of the earthquake for each individual line affected by the earthquake (i.e., those near the epicenter). These offsets are then subtracted from the original line length data and a "reduced" set of measurements is created. Great care must be taken to ensure that the offsets determined in this way are reasonable by checking that the pattern of offsets makes sense with respect to the known faulting. Largely, this was done using forward modeling with an elastic dislocation code to assure ourselves that each offset was plausible. We have tried to be conservative in our approach, and have fit for coseismic offsets only on those lines which clearly have been disturbed by the earthquakes. Effects from a total of seven earthquakes were removed by this process: 1979 Homestead Valley (M_L 5.2), 1979 Imperial Valley (M_L 6.6), 1979 Brawley (M_L 5.5), 1981 Westmorland (M_L 5.7), 1986 North Palm Springs (M_L 5.9), 1987 Elmore Ranch (M_L 5.8), and 1987 Superstition Hills (M_L 6.0). These earthquakes and their location with respect to the Geodolite network are shown in Figure 2.

The majority of these large earthquakes were in the Imperial Valley, where triggered surface slip is often observed on faults far from the earthquake epicenter [e.g., *Allen et al.*, 1972]. The Geodolite data show that secondary deformation of this style occurred at a measurable level for the Imperial Valley/Brawley earthquake pair and also for the Elmore Ranch/Superstition Hills pair. The triggered slip at the time of the Imperial Valley earthquake was on the Superstition Hills Fault near the Geodolite station SUP (see the index map, Figure 2, for the location of stations named in the text) and produced small offsets on all lines into SUP which had the same sense as the coseismic offsets 8 years later when this fault, itself, ruptured. Triggered slip caused by the Superstition Hills earthquake occurred along the southern San Andreas Fault and caused the station at Bat Caves Buttes, SALTON, to move toward the southeast; just the direction expected due to the stress buildup on this

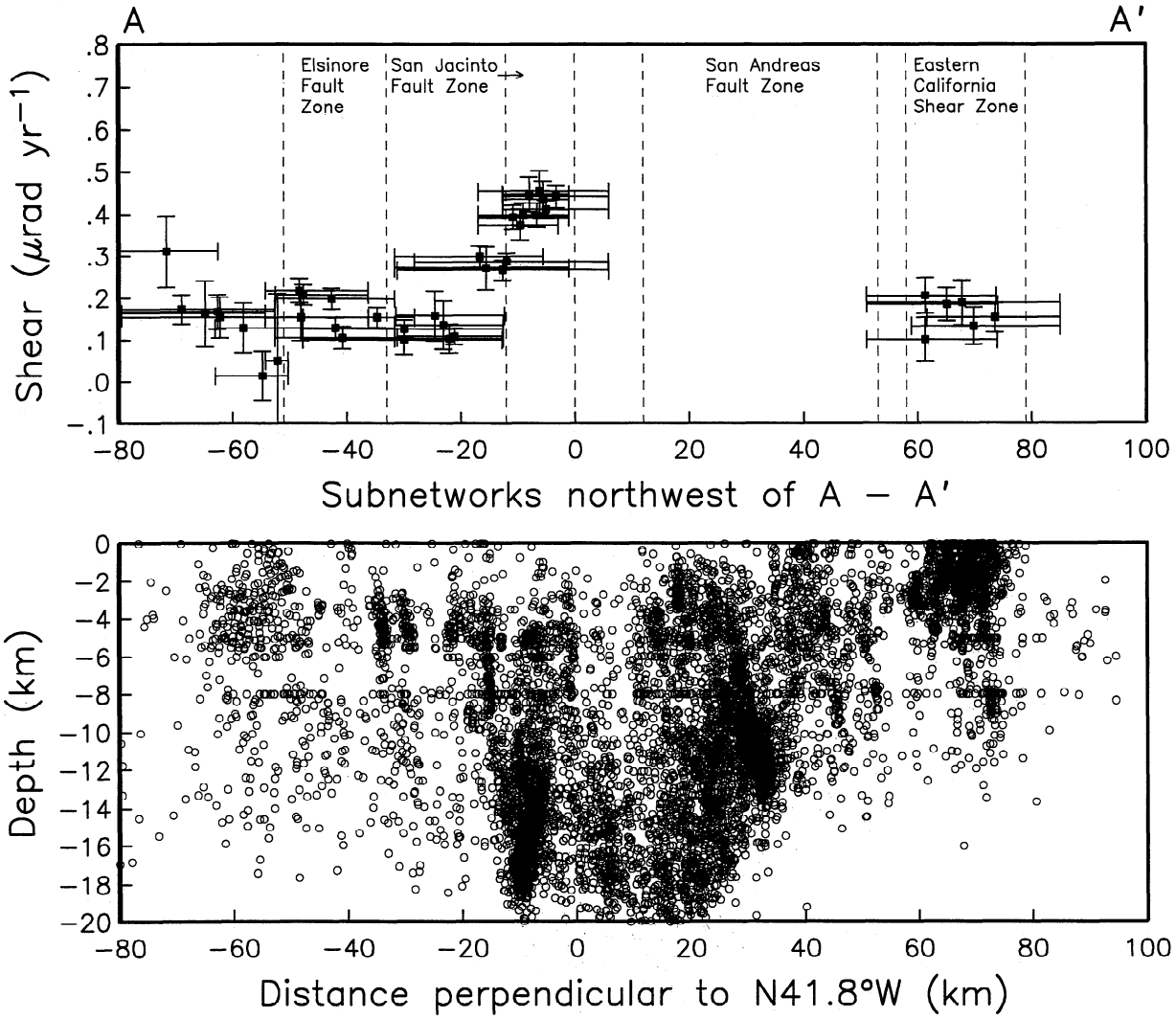

Figure 9. Engineering shear strain rate profile perpendicular to local faulting in the northwest Anza and Joshua Tree networks (above), and depth profile of quality A and B earthquakes from the Caltech catalog from 1973 through 1991. All strain rate estimates from the four-station subnetworks northwest of the line A to A´ in Figure 7 were resolved into right-lateral shear strain rate at an azimuth of N41.8°W. This is the azimuth of maximum shear strain rate for the combined Anza and Joshua Tree subnetworks. The San Andreas fault zone appears as a smeared-out feature in this plot because the fault is not perpendicular to N41.8°W.

section of the fault. We have fit for these two sets of offsets in the raw line length data in the same manner as for the seven large earthquakes discussed above.

Since the aim of this paper is to better understand the accumulation of interseismic strain, these earthquake-related offsets are an unwanted complexity. However, the assumptions made here identify such anomalies well; for other researchers who may be studying these events in detail, our offset estimates are tabulated by *Johnson* [1993].

Besides these earthquake related offsets, we found only one Geodolite station, near the town of Anza, which clearly was affected by "something." There are no recorded earthquakes which can account for this single offset on the line between stations ROAD and THOM-CGS, occurring sometime between late 1975 and late 1977, and the event does not seem to be of any other tectonic origin. Nonetheless, we allowed our routines to fit an offset on this single line during this period of time. We also detected two length measurements on separate lines which we believe to be blunders of one sort or another: the 1974 measurement between stations ASBESRM1 and TORO, and the 1987 measurement between stations BLUFFRM1 and OCOTILLO. These are the only two measurements which were actually removed from the data.

This editing process is somewhat different from that used by *Savage et al.* [1986] and *Lisowski et al.* [1991]. In each of those studies all observations which fell more than three standard deviations away from the best linear fit to the remaining data for each Geodolite line were removed, resulting in many more rejected data than our approach.

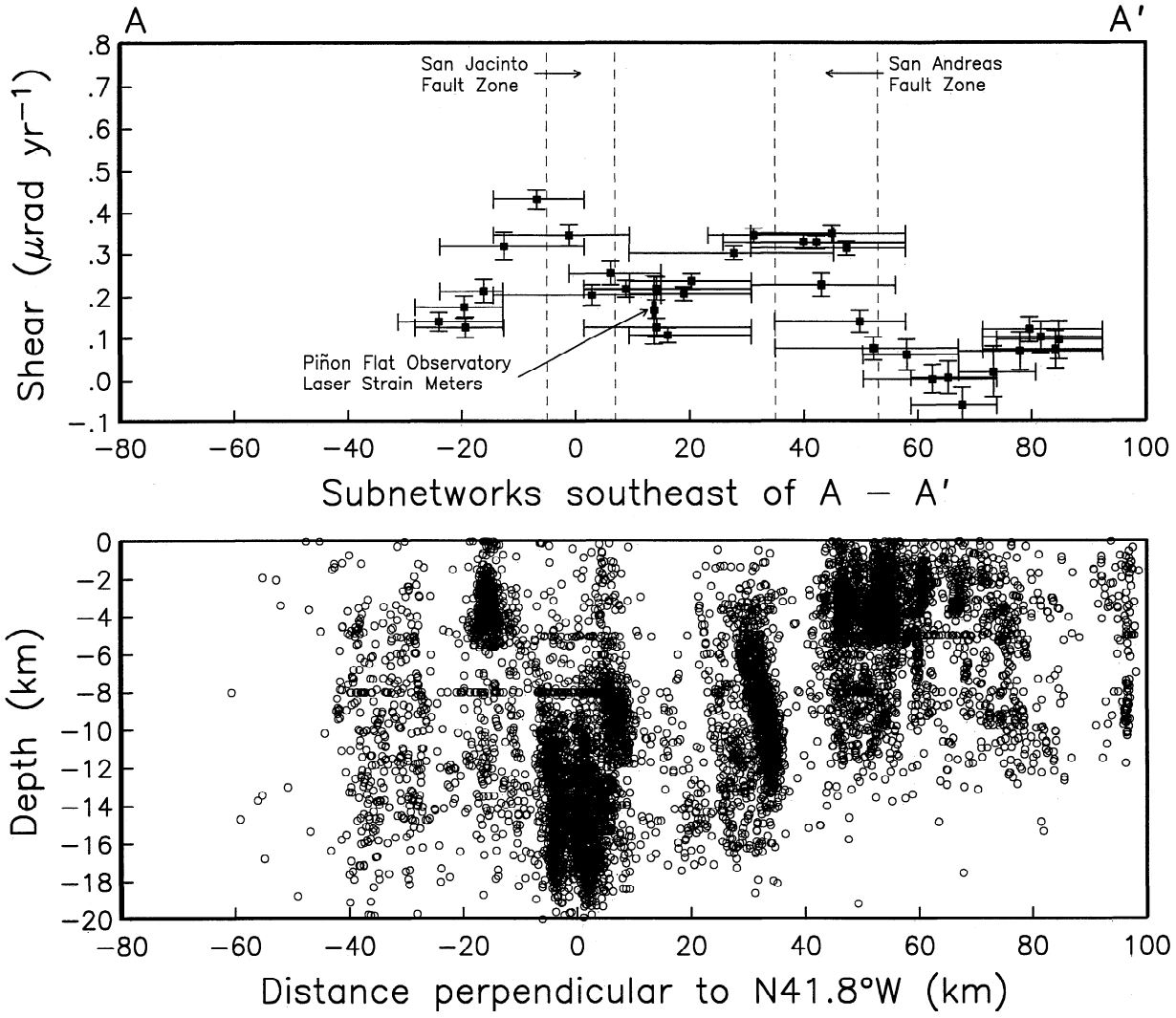

Figure 10. Engineering shear strain rate profile and seismicity for all four-station subnetworks of the Anza and Joshua Tree subnetworks southeast of the line A to A′ in Figure 7.

Savage et al. [1986] show that the number of measurements removed by this procedure is consistent with the number of observational blunders expected from this type of field program. There is no obvious reason to prefer one technique over the other, and our choice was largely influenced by a desire to judge the data in a different way specifically to see if the final results would be similar. In the end, our editing technique left us with 1932 line length observations spanning 18 years of field work on 202 lines between the 95 stations shown in Figure 1.

There are two locations in the combined Anza, Joshua Tree, and Salton Geodolite networks where multiple geodetic markers exist near one another but are not tied together. In each case this is simply due to the topography of the areas and the need for the Geodolite equipment to have direct line of sight to make its measurements. We have assumed that negligible displacement occurred between each set of these nearby sites over the entire duration of the program and combined the sites into one so that a strain rate tensor could be determined. The three individual sites on the top of Thomas Mountain, in Riverside County, are within about 500 m of one another, while the two sites on Santiago Peak, in Orange County, are about 200 m apart. In each case, due to the stable geology of the nearby areas and the lack of any active faults, we believe that the assumption of negligible relative displacement is reasonable.

Error Estimates

As discussed in the introduction, *Savage et al.* [1986] suggest that the overall uncertainty in an individual Geodolite measurement can be represented by equation (1) with $a = 3$ mm and $b = 0.2$ ppm. We would like to make an independent estimate of these terms from the reduced data discussed above, and in particular we would like to estimate the survey-to-survey systematic error components so that they can be removed before the strain rate tensors are calculated.

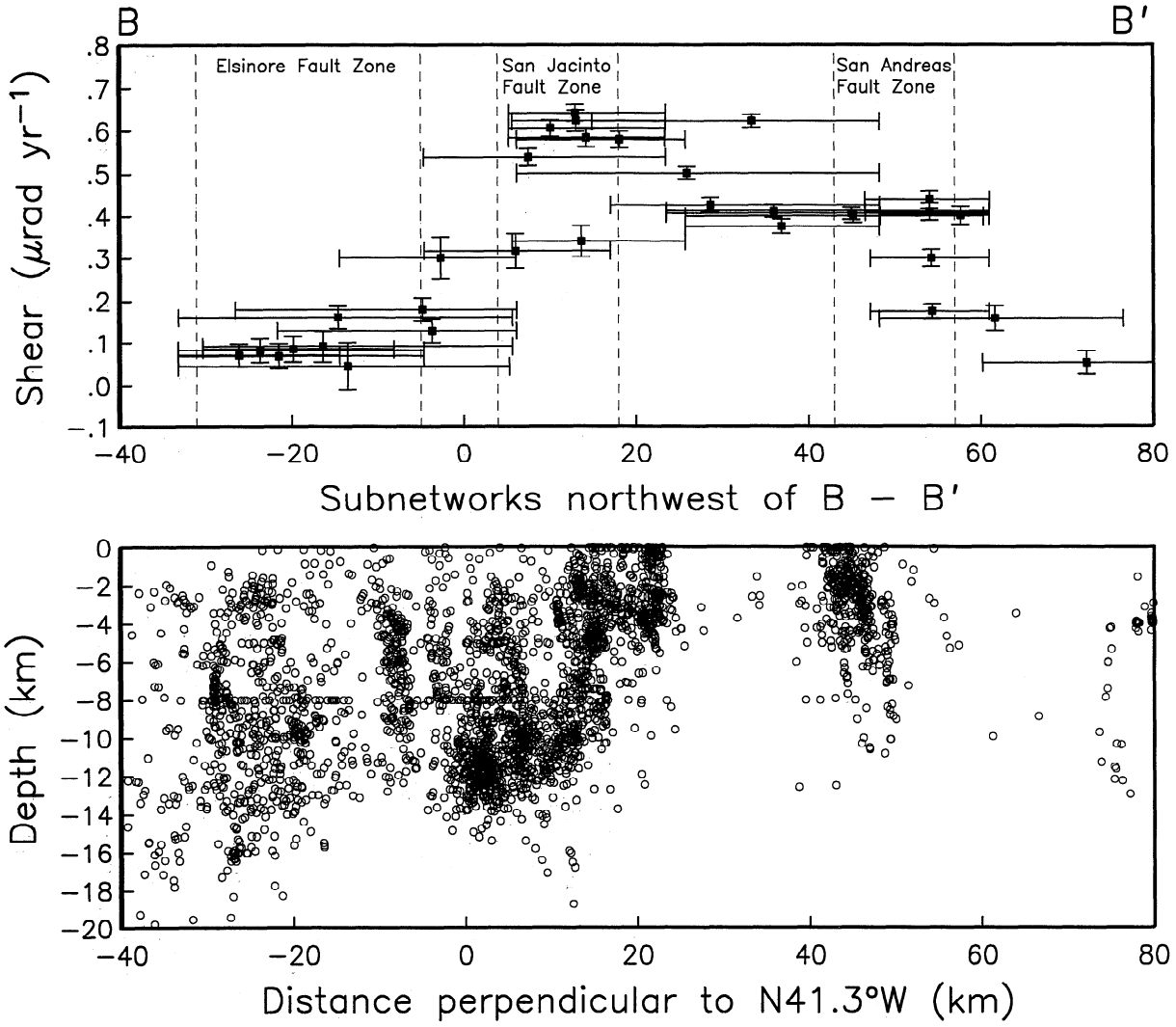

Figure 11. Engineering shear strain rate profile and seismicity for all four-station subnetworks of the Salton subnetwork northwest of the line B to B´ in Figure 7. The azimuth of maximum shear strain rate for the Salton subnetwork is N41.3°W.

To begin, a best fit linear regression of distance versus time is calculated for each of the lines in the network using a least squares technique, and the residuals from this linear fit are plotted for all 1932 line length observations, as in Figure 3. (We have also used other, more robust, line fitting routines, such as a one-norm misfit criterion, or by assuming the error distribution is even more heavy-tailed by assuming a Lorenzian error distribution [see *Press et al.*, 1987]. The results turn out to be nearly identical in each case, and so we present only the least squares results.) As evident in Figure 3, the data are bunched in time at approximately yearly intervals because the field crew would typically resurvey the southern California networks all at once during the winter months. What is important here is that the yearly residuals are often offset from zero and do not extend evenly above and below zero; this is a manifestation of the systematic errors due to miscalibrations in the meteorological and EDM gear. (It is also possible, though highly unlikely, that these "scale" errors from year-to-year are due to region-wide areal extensions and contractions.)

To estimate the systematic error terms for each of the surveys, we plot the residuals for one survey versus their line length, as in Figure 4 for the 1978 survey, and estimate the slope and intercept of a linear fit using a least squares technique. By repeating this process on each of the other yearly surveys we determine the estimates of systematic error shown in Table 1. These 38 data taken together suggest that a_s is well described by a normally distributed random variable with mean 0.12 mm and standard deviation 1.8 mm; that is, the a_s is distributed as N(0.12 mm, 1.8^2 mm^2). Similarly, b_s is distributed as N(0.026 ppm, 0.15^2 ppm^2). *Savage et al.* [1986] estimate these two terms to be N(0 mm, 0.5^2 mm^2) and N(0 ppm, 0.14^2 ppm^2), respectively, from a series of calibration tests. Only our estimate of the variance in the constant term is significantly different from those of *Savage et al.* [1986]. We have used the values in Table 1 to remove these systematic effects from the reduced data and call this our "final-reduced" data. The resulting plot of residuals with respect to a linear accumulation of strain, versus the time of each

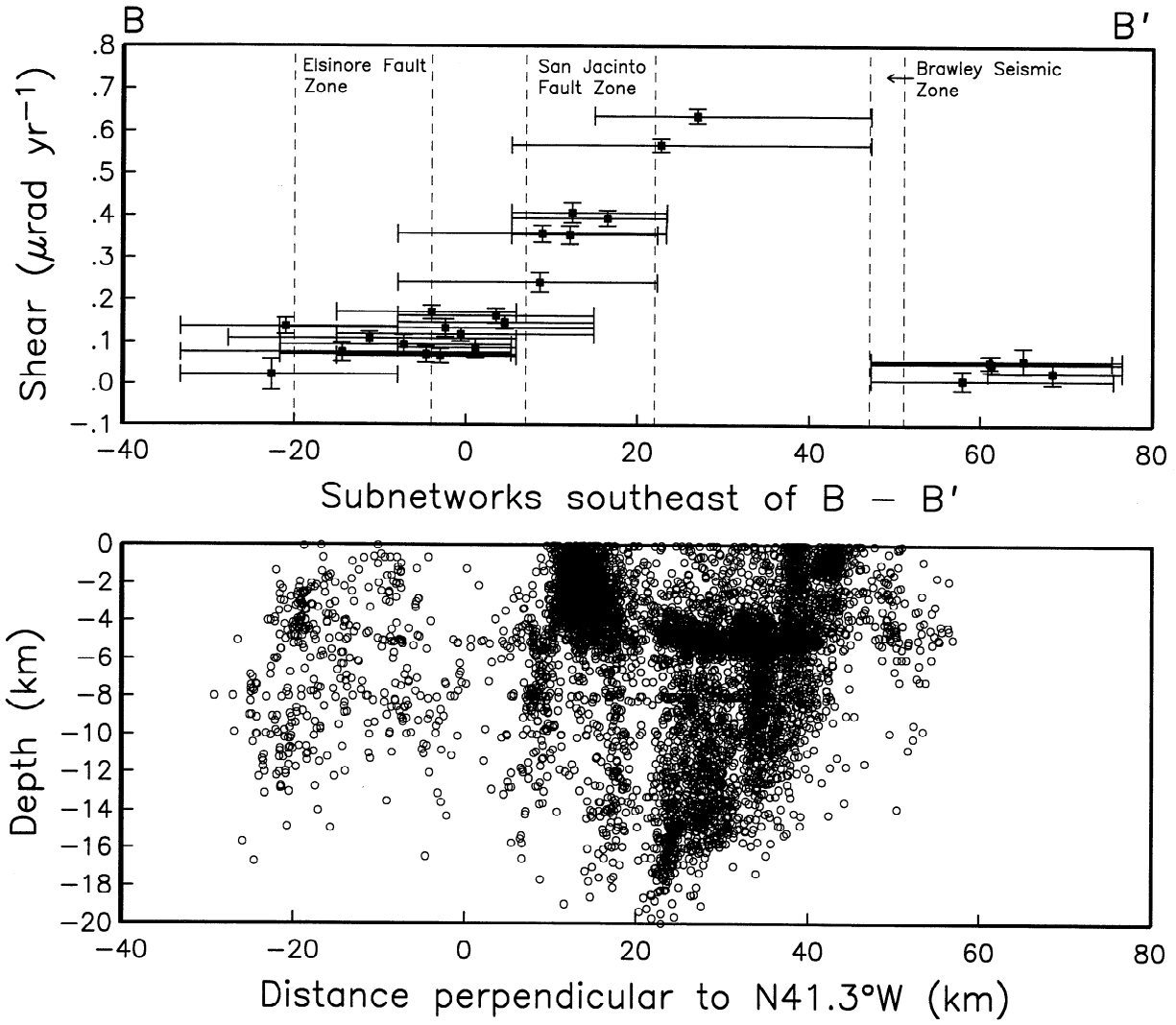

Figure 12. Engineering shear strain rate profile and seismicity for all four-station subnetworks of the Salton subnetwork southeast of the line B to B′ in Figure 7.

measurement, is shown in Figure 5 (compare with Figure 3). As expected, the residuals are now much more evenly distributed above and below zero.

We now wish to investigate the purely random errors remaining in Figure 5 (as opposed to the systematic errors discussed above). As suggested by equation (1), we need to estimate the variance of the Geodolite measurements as a function of line length. This information is already contained in Figure 5, but in a different format. For each Geodolite line we take the corresponding residuals from Figure 5 and determine their variance. These values are then plotted versus the square of the length of each of the lines, as in Figure 6. The trend in this plot is for longer lines to have larger variances, though this correlation is not particularly strong. The individual lines which correspond to the 10 circled data points in the upper left part of the plot have anomalously large residuals during the 1981 through 1984 surveys. The surveys during these years were contracted to non-USGS field crews and are suspected of containing more outliers than usual (M. Lisowski, personal communication, 1993). We therefore feel justified in removing these 10 points before the best fitting constant error and length-dependent error terms are determined. (These 10 data points come from lines which are randomly distributed throughout the overall network and are not concentrated in any one geographic area. They have not been used when estimating the random error terms below, but the lines from which these points are derived have not been removed from the data.) We find the best estimate for a_r to be 3.8 mm and the best estimate for b_r to be 0.16 ppm. *Savage et al.* [1986] estimate these terms as 3 mm and 0.14 ppm. As with the systematic error terms above, we find that our value for the constant term is slightly larger than previous estimates, while the length-dependent terms agree quite well.

Since we have removed the systematic error sources from our final reduced data to the best of our ability, we are left with only the random component of error to assign to each of the individual Geodolite measurements. We have therefore used equation (1) with $a = 3.8$ mm and $b = 0.16$

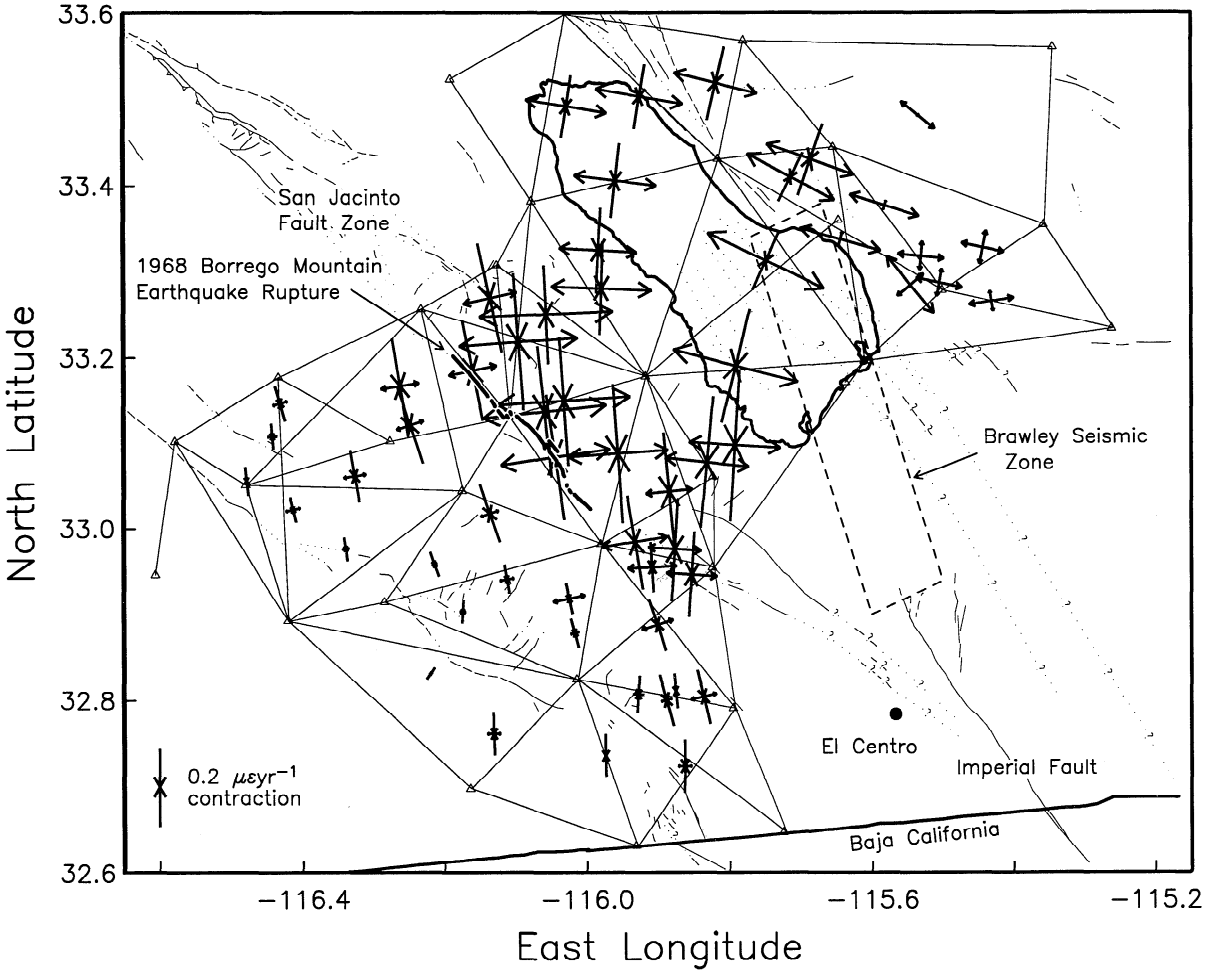

Figure 13. Close-up view of the principal strain rates in the Salton subnetwork.

ppm in our calculations below of the horizontal strain rate tensors.

Results and Discussion

Figure 7 presents the primary results of this study as a map of the present-day strain accumulation (18-year average) across the southern California region. The principal strain rates for each four-station subnetwork are plotted at the geometric center of the subnetwork. We have computed these strain rate estimates for all possible subnetwork combinations of four stations, and so there is some overlap of results in areas where the network is extensive. This region-wide view of the strain rate estimates makes it possible to see the overall pattern of deformation and how it relates to the tectonics of the area (closeups are presented later in the paper). Principal strain rates for each of the four-station subnetworks are tabulated at the end of the paper in Table 2 and Figure 20.

Figure 8 contains the same basic information as Figure 7 but in a different format. Figure 8 plots the individual linear strain rates for all lines in the Geodolite network, with solid lines representing extension and dashed lines representing contraction. The thickness of each line is proportional to the rate at which strain is accumulating. Essentially, the results in Figure 8 are the inputs to the tensor calculations, the results of which are plotted in Figure 7. The dominant feature seen in Figure 8 is that the majority of lines directed approximately north-south are contracting while lines directed approximately east-west are extending.

The median size of the strain rates presented in Figure 7 is about 0.11 $\mu\varepsilon$ yr^{-1}, while the median strain rate uncertainty is about ± 0.02 $\mu\varepsilon$ yr^{-1} resulting in a median signal-to-noise ratio of about 6. The median uncertainty in the azimuth of the principal strain rate estimates is $\pm 4°$. Many of the uncertainties in both magnitude and azimuth are quite a bit smaller than these values, especially in the southern part of the network near the Salton Sea, as well as along the entire length of the San Jacinto fault zone. There are two areas in the overall network where the uncertainties are consistently larger than elsewhere in the network: at the western and northern extremes. Both of these areas were surveyed approximately half as often as the remainder of the network so that the larger uncertainties are simply due to a relative lack of data.

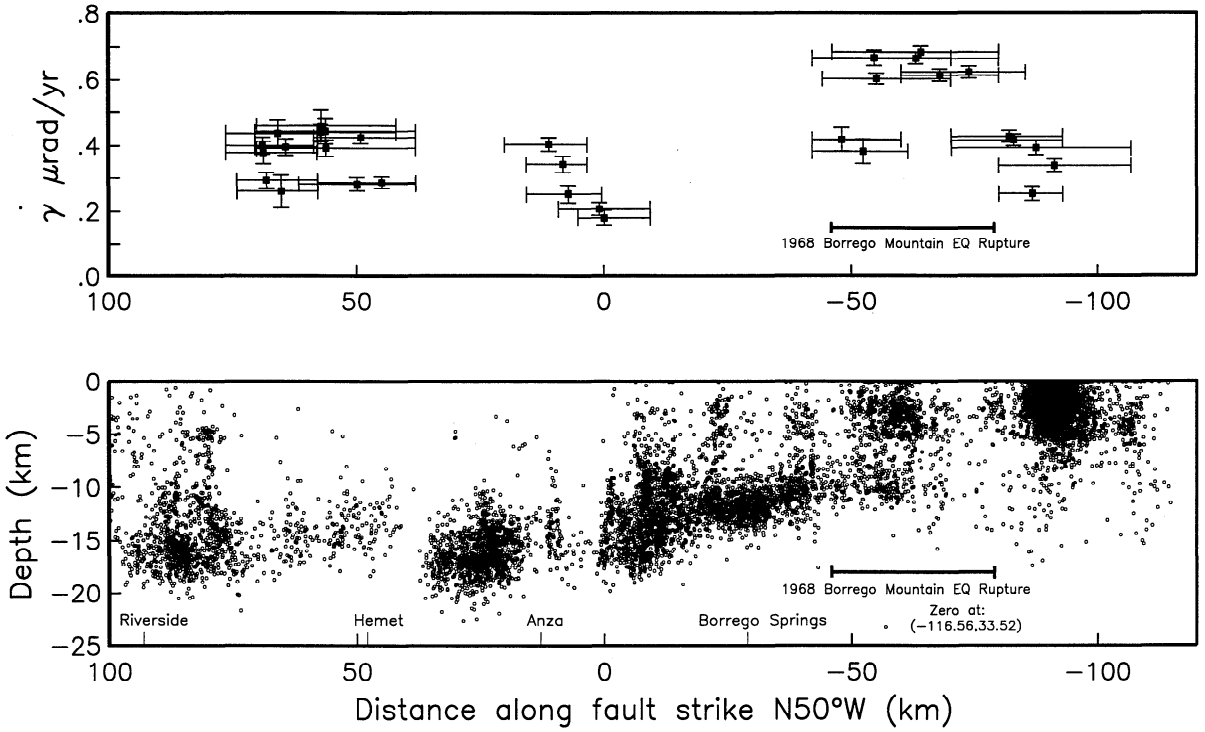

Figure 14. Fault-parallel engineering shear strain rate for Geodolite subnetworks located along the trace of the San Jacinto Fault (above) and seismicity from the Caltech catalog from 1976 to 1991, projected onto the fault face (view is from the southwest). The progressive shallowing of earthquake hypocenters to the southeast is consistent with interseismic slip shallowing as well. The location of the subnetworks with high strain rate is well correlated with the 1968 Borrego Mountain surface rupture.

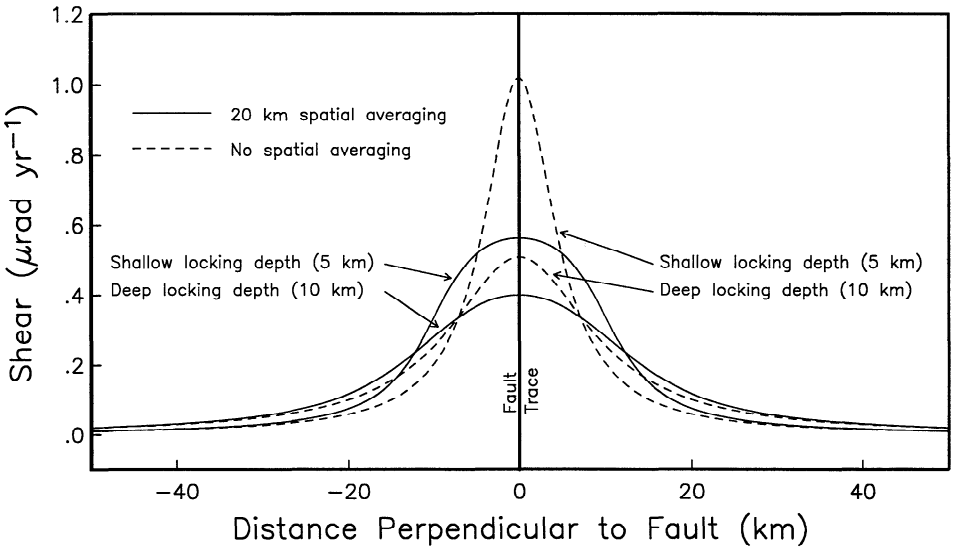

Figure 15. Right-lateral engineering shear strain rate parallel to a modeled strike-slip fault (from equation (3)). The simple dislocation model assumes an elastic half-space with a buried straight fault locked from the surface to some depth and slipping freely below at a steady rate. The "deep" locking depth is 10 km (to model the northern San Jacinto Fault, see text) while the "shallow" locking depth is 5 km (southern San Jacinto Fault). The four-station subnetworks of Geodolite data average over about a 20-km-wide zone (solid lines). The dashed profiles assume no spatial averaging (i.e., point strain rate measurements) and are for comparison.

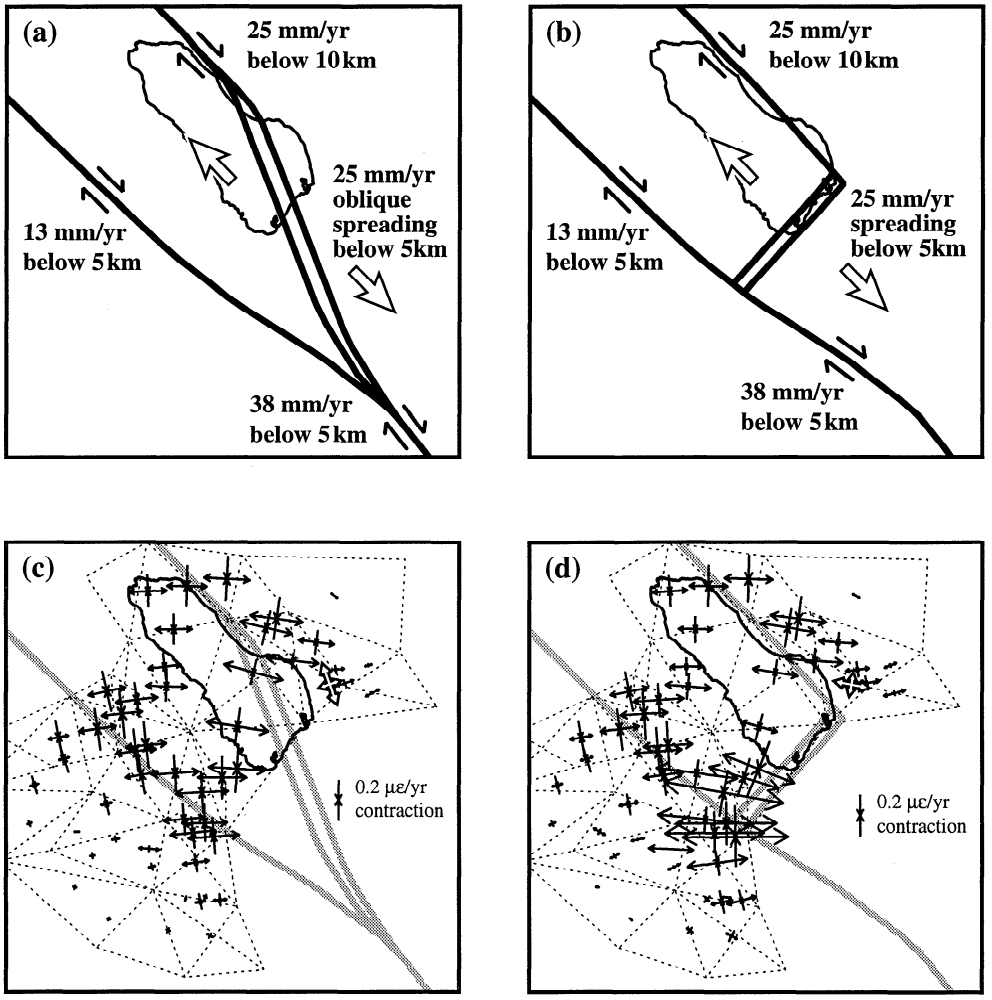

Figure 16. Two possible kinematic models for slip transfer (a) and (b) between the southern San Andreas Fault and the Imperial Fault and (c) and (d) the surface strain rates resulting from these models. Approximate slip rates and locking depths are from *Bird and Rosenstock* [1984], *Weldon and Sieh* [1985], *Johnson et al.* [1990], *Rockwell et al.* [1990], and *Sieh and Williams* [1990]. Each model predicts a single dilatational strain rate result east of the Salton Sea (highlighted) as compared to the seven dilatational results seen in the Geodolite data (Figure 13). The "stair-step" model predicts far too much east-west extension and not enough north-south contraction in the area south of the Salton Sea. Results from the "oblique" model match Figure 13 more closely.

Overall Patterns of Deformation

There are many interesting features in Figures 7 and 8 which provide an understanding of the present-day crustal deformation in southern California. Perhaps the most obvious aspect of Figures 7 and 8 is simply that there are many coherent patterns visible. For instance, areas of high strain rate slowly grade to areas of lower strain rate, and these correspond well with the tectonic features of the region: large strain rates along the major faults and smaller strain rates between the faults.

A close inspection of the azimuths of the principal strain rates in Figure 7 shows that these directions change coherently as the fault traces bend throughout the region. Theoretically, a vertical strike-slip fault buried in an elastic half-space and allowed to slip at depth while staying locked near the surface will produce pure shear strain at the surface (depicted in the inset in Figure 7) with the principal axes at 45° to the fault trace. In Figure 7 the plotted strain rates are indeed almost always at 45° to the local fault trace and the vast majority of the subnetwork results show nearly pure shear. For example, in the region around the Salton Sea, the San Jacinto Fault and the San Andreas Fault are not quite parallel, the San Jacinto pointing more westerly and the San Andreas more northerly (this can be seen more clearly in the close-up in Figure 13); the principal strain rates are rotated more westerly over the San Jacinto and more northerly over the San Andreas, with a smooth progression of azimuths between the two areas. Farther northwest along the San Andreas, just east of Palm Springs, near where the San Andreas bends to the west as it heads toward the Transverse Ranges, the axes of the principal strain rates

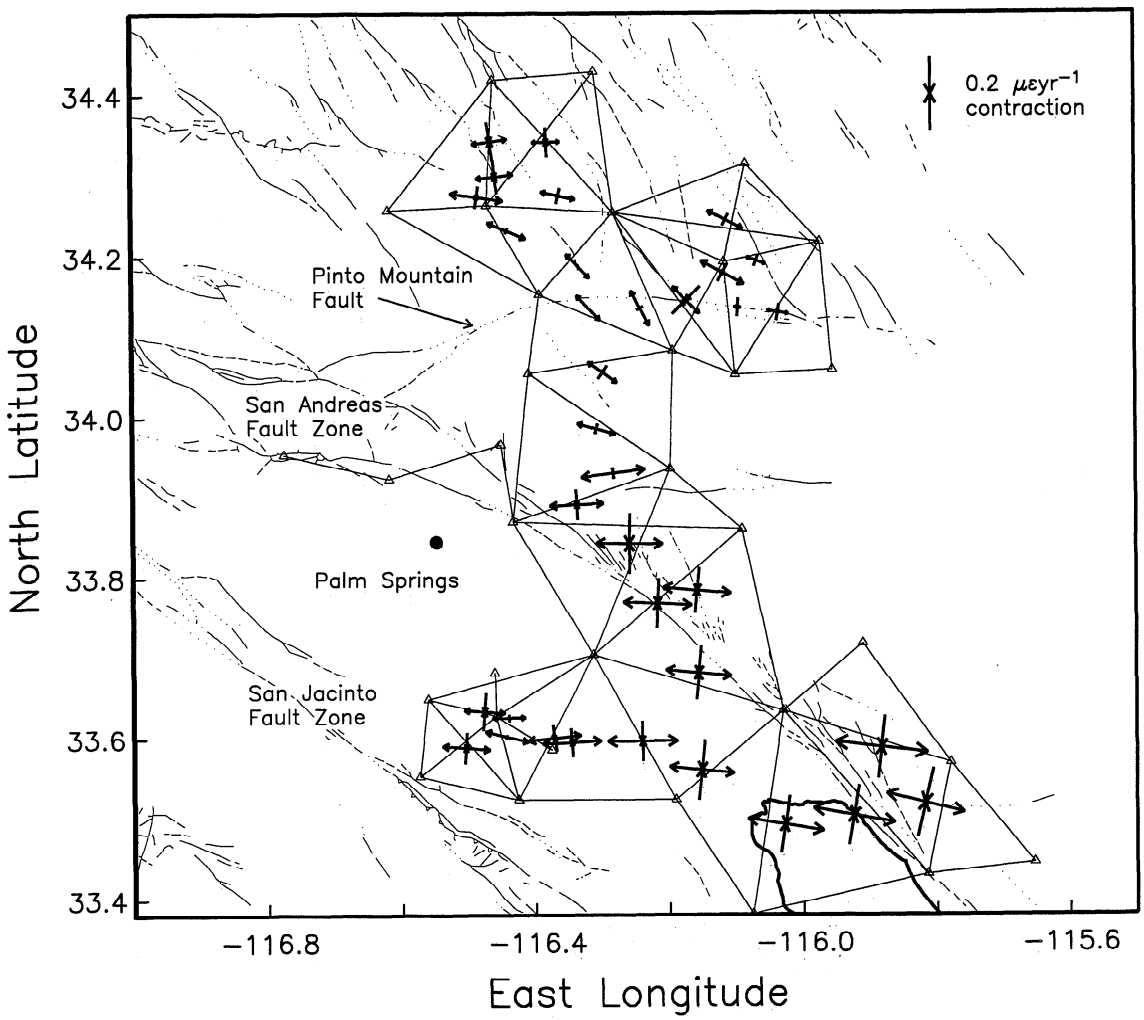

Figure 17. Close-up view of the principal strain rates in the Joshua Tree subnetwork.

also rotate to the west. Additional examples can be seen throughout the region.

One of the most apparent results in Figure 7 is that the largest strain rates in the entire southern California region are along the San Jacinto Fault southwest of the Salton Sea. This area shows nearly pure shear with the axis of maximum contraction directed from slightly west of north to slightly east of north at a level of up to 0.35 $\mu\varepsilon$ yr^{-1}. The next largest zones of strain accumulation are along the southernmost extent of the San Andreas Fault along the eastern shore of the Salton Sea and also along the two northern sections of the San Jacinto Fault, south and west of Palm Springs; these rates reach approximately 0.25 $\mu\varepsilon$ yr^{-1}. The surprising aspect is that it is the San Jacinto Fault which dominates and not the San Andreas. To be sure, the amount of strain accumulating on the southern San Andreas Fault is large, but everywhere the Geodolite data cross the San Jacinto Fault the strain rate results are at least as large, and the results are significantly larger along the Imperial Valley segment of the San Jacinto.

The strain rate results in Figure 7 represent a spatial average of the actual strain rate in Earth's crust within each subnetwork. Because we expect the actual strain rate to vary throughout the region, especially in relation to the location of the major faults, this is an important consideration when making comparisons between rates in different parts of the network. The median fault-perpendicular averaging width of the 131 subnetworks represented in Figure 7 is about 22 km. For those subnetworks along the length of the San Jacinto Fault the typical averaging width is similar at about 23 km, while the subnetworks along the San Andreas Fault extend about 21 km perpendicular to that fault. Individual subnetworks obviously vary from these values, but a detailed comparison between the San Jacinto and San Andreas subnetworks (not included here) shows that the distributions are very similar and that there is no obvious correlation between narrower averaging widths and higher strain rates. Thus the design of the Geodolite network is not responsible for the larger strain rates along the San Jacinto Fault.

Across-Axis Strain Rate Profiles

To understand further the relationship between the deformation estimates and the fault zones throughout southern California, Figures 9-12 present across-fault-axis

profiles of the (approximately) fault-parallel engineering shear strain rate and depth profiles of seismic activity for the duration of the Geodolite program (these may be compared with the works by *King and Savage* [1983] and *Lisowski et al.* [1991]). The data from the Anza and Joshua Tree regions, northwest of the "waist" in the network at the northern tip of the Salton Sea (see Figure 2 for the location of this waist), are projected onto the line A to A′ of Figure 7, while the Salton Sea area data are projected onto the line B to B′. The azimuth of these projections was determined by finding the direction of maximum shear strain rate for all data northwest and southeast of the waist. These azimuths turn out to be about the same in the two areas. In the northwest area the direction is N41.8°W ±0.6°, and in the southeast area it is N41.3°W ±0.7°. Because these azimuths are not exactly parallel to the local strike of the major faults (they differ by as much as 10°), the dashed fault zones plotted in the top panel of each figure show the extreme fault zone locations. The horizontal error bars on the data show the lateral extent of the four-station subnetworks.

An interesting feature of these across-axis shear strain rate profiles is that where the four-station subnetworks cross the San Jacinto and San Andreas Faults the zone of strain accumulation is quite wide. Naturally, some of this broad character is due to the spatial averaging of the subnetworks, but the closeness, and therefore interaction, of the two faults is also an important factor. In the northern part of the network (Figure 10) there are two distinct peaks in the shear strain rate over the San Jacinto and San Andreas with each zone of deformation about 35 km wide, while farther southeast (Figure 11) the two peaks have merged into one larger peak of approximately 60 km width, with a hump on the northeast side above where the San Andreas is located. Still farther to the southeast (Figure 12) the zone of deformation has shifted somewhat to the northeast of the San Jacinto fault zone and narrowed to about 45 km.

We have included an additional strain rate result in Figure 10 from the laser strain meters at Piñon Flat Observatory (the location of the observatory is shown in map view in Figure 19) for the period 1985 to 1990. This measurement period overlaps with the last 6 years of Geodolite measurements. The value of 0.17 ± 0.08 μrad yr^{-1} agrees well with the Geodolite results and is about half of the peak strain rate directly above either the San Jacinto or San Andreas Faults. It is worth pointing out that the laser strain meter measurements are made over baselines of approximately 700 m and so are essentially point results given the scale of Figure 10.

Change in Strain Rate Along the San Jacinto Fault

As shown in Figure 7, the largest strain rates in the southern California region occur along the San Jacinto Fault southwest of the Salton Sea (a close-up view of this area is shown in Figure 13). There is a gap in the geodetic coverage for about 30 km to the northwest along this fault, where the network again crosses the fault both south and west of Palm Springs (see Figure 19 for a close-up). The strain rates in these second two regions are about two thirds as large as the strain rates in the Imperial Valley area. This can be seen more clearly in Figure 14 where the fault-parallel shear strain rate is plotted along the length of the San Jacinto Fault. Only those subnetworks which are directly above the San Jacinto are included in Figure 14. At first, one might think this is clear evidence that the amount of steady interseismic slip changes along the length of the fault; for instance, there could be about 10 mm yr^{-1} of slip on the northwest sections of the fault [*Sharp*, 1981; *Rockwell et al.*, 1990] and 15 mm yr^{-1} on the Imperial Valley segment. If this is the case, it leads to a problem: where does the extra slip go? Schemes can be created where this excess slip is somehow transferred to (say) the San Andreas Fault across the northern Salton Sea, but we are unaware of any geological evidence for such a transfer of displacements.

Another possibility is that the amount of slip along the length of the San Jacinto is approximately the same, and it is only the depth at which this slip occurs that changes. To demonstrate how this works, we resort to a very simple model of strike-slip fault behavior; we assume Earth is a purely elastic half-space with an infinitely long, straight fault embedded in it, which is locked from the surface to a depth of H kilometers and slips at a steady rate of S meters per year below this depth. For this model the rate of engineering shear strain at the surface is

$$\dot{\gamma} = \frac{-2S}{\pi} \frac{H}{H^2 + x^2}, \tag{2}$$

where x is the distance perpendicular to the fault. The four-station subnetworks that are used to calculate the strain rates in our figures average this strain over approximately a 20-km-wide zone, so we really must determine the spatially averaged shear strain rate, which is

$$\langle \dot{\gamma} \rangle = \frac{\frac{-2S}{\pi} \int_{x_1}^{x_2} \frac{H}{H^2 + x^2} dx}{x_2 - x_1}$$

$$= \frac{-S}{\pi(x_2 - x_1)} \left[\tan^{-1}\left(\frac{x_2}{H}\right) - \tan^{-1}\left(\frac{x_1}{H}\right) \right], \tag{3}$$

where angle brackets indicate the spatial average.

If we assume that the rate of slip along the San Jacinto fault is constant for its entire length and that it is occurring below about 10 km on the northwest segments (as suggested by the seismicity in the bottom panel of Figure 14) and use a subnetwork width of 20 km, we can then determine an effective locking depth for the southeast portion of the fault. We find the locking depth must be about half as deep on this segment, or 5 km, to explain the observed two-thirds discrepancy in shear strain rate. The seismicity in Figure 14 shows this to be a reasonable possibility: the seismogenic depth progressively shallows to the southeast in this plot (see also *Sanders and Kanamori* [1984]). Figure 15 presents a profile of the shear strain rate of equation (3) for both the 10 km (deep) and 5 km (shallow) values. The solid profiles use a spatial averaging width of 20 km, while the dashed profiles use no spatial averaging at all (i.e., point strain rates). These profiles can be compared to Figures 10 and 11.

A third possible explanation for the large amount of deformation along the southern San Jacinto Fault is acceler-

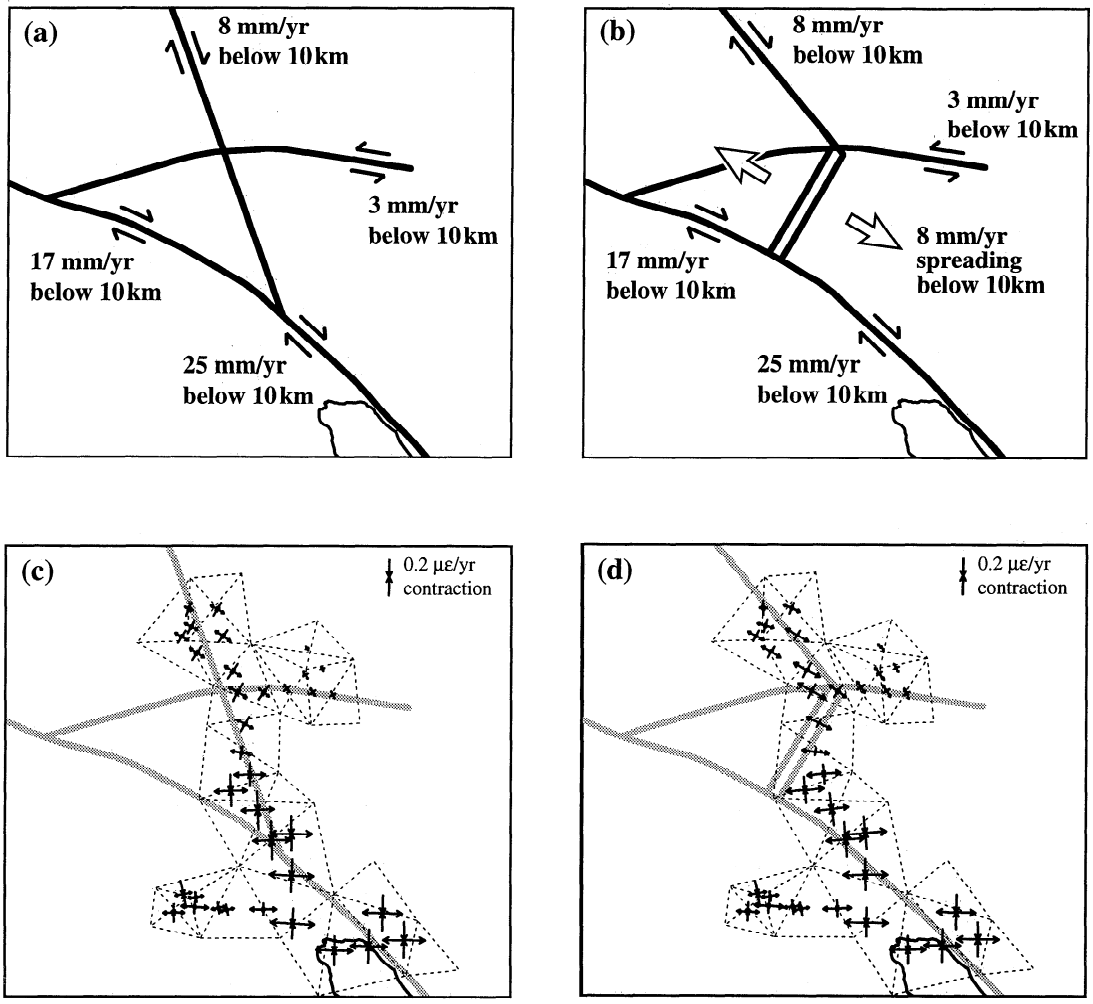

Figure 18. Two possible models for the diversion of deformation (a) and (b) away from the southern San Andreas Fault and into the Eastern California Shear Zone and (c) and (d) the surface strain rates resulting from these models. Approximate slip rates and locking depths are from *Bird and Rosenstock* [1984], *Weldon and Sieh* [1985], *Johnson et al.* [1990], *Savage et al.* [1990], and *Sieh and Williams* [1990]. The left model predicts essentially pure shear strain rates throughout the region (because it involves only transcurrent faulting) and is unable to reproduce the zone of almost pure extension between the San Andreas and Pinto Mountain Faults while the right model, because of the small spreading center, comes quite close to reproducing the Geodolite results (compare to Figure 17).

ated strain accumulation as an aftereffect of the 1968 Borrego Mountain earthquake. The approximate location of the surface rupture caused by this earthquake is shown as a bold line in map view in Figure 13 near station OCOTILLO and in profile in Figure 14. *Thatcher* [1983] showed that a combined set of geodetic measurements from networks along the entire length of the San Andreas Fault in California are supportive of the possibility that surface deformation follows a nonlinear accumulation during the interseismic period of the earthquake cycle, with relatively high rates immediately after a large earthquake decreasing to much lower rates late in the cycle. He determined a time constant of about 30 years for this effect based on either a modified elastic half-space model with a time-variable rate of interseismic slip or a model with viscoelastic coupling between the lithosphere and asthenosphere [see Thatcher, 1983, Figure 11, p. 5897]. On the other hand, *Savage et al.* [1986] have shown that the Geodolite data used here are consistent with a purely linear accumulation of deformation. Of course, this 18-year span of measurements is unable to distinguish between a linear accumulation of strain and a nonlinear accumulation with an appropriately long time constant. In this case, the Geodolite measurements place a lower bound on the time constant for the San Jacinto Fault which will be considerably longer than the estimate of 30 years determined by *Thatcher* [1983] for the San Andreas Fault.

One observation in favor of accelerated strain accumulation is the detailed distribution of the subnetworks along the southern San Jacinto Fault which show high strain rates. The strain rates along the entire San Jacinto are generally between about 0.3 and 0.4 μrad yr^{-1} except for the six sub-

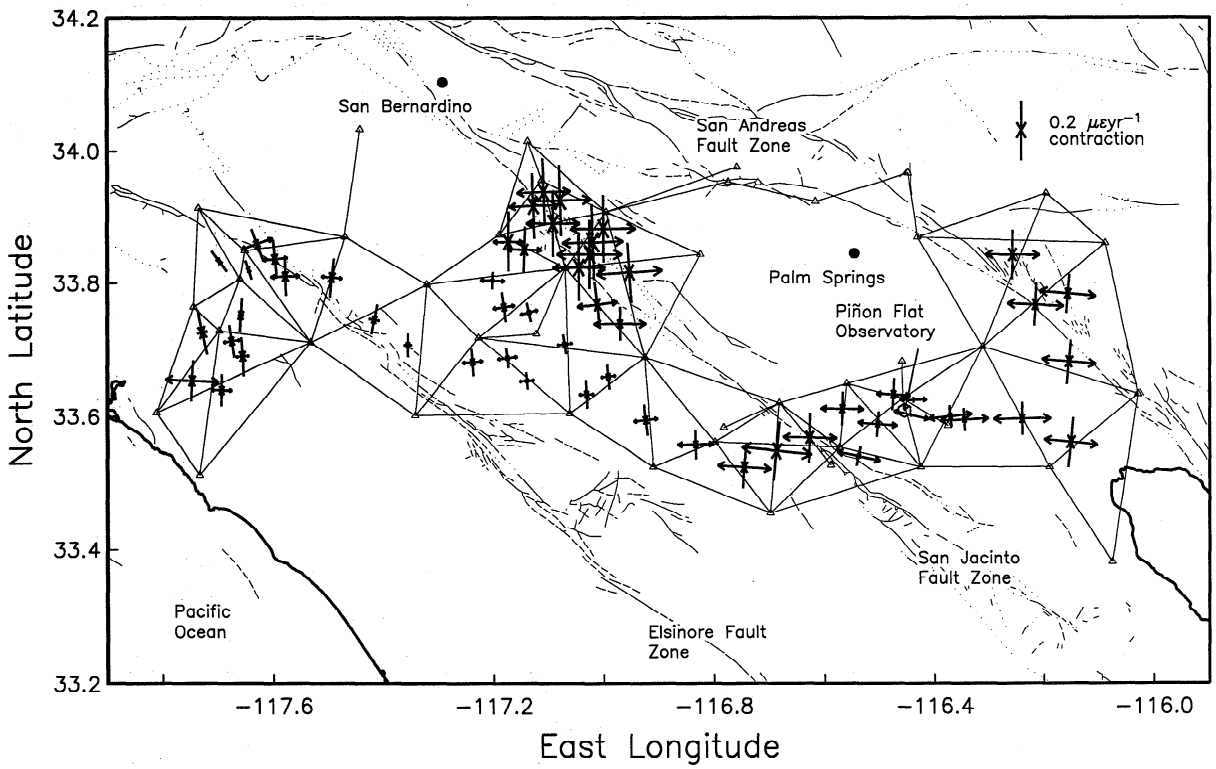

Figure 19. Close-up view of the principal strain rates in the Anza subnetwork.

networks that correspond to the 1968 rupture (see Figure 14) which have values between 0.6 and 0.7 μrad yr^{-1}.

We cannot prove that one of these possibilities is correct and the others incorrect using only the Geodolite data. It is likely that these high strain rates are due to a combination of a shallowing in the depth of subsurface motion along the length of the San Jacinto Fault toward the southeast and accelerated strain accumulation following the Borrego Mountain earthquake.

Spreading Center Beneath the Salton Sea

Another unexpected pattern of deformation can be seen east of the southern tip of the Salton Sea (Figure 13) where the southern San Andreas Fault makes its transition to the Brawley Seismic Zone. Careful examination of the strain rate results shows that seven of the subnetworks in this area are experiencing areal dilatation with little shear; that is, the surface of the earth is extending in both principal directions. This can also be clearly seen in the individual linear strain rate results in Figure 8. All Geodolite lines in this area are extending, regardless of their azimuth. This is not expected in an area of transcurrent faulting where pure shear results should dominate. This is the same area where *Reilinger* [1985] found an anomaly in the vertical deformation field from leveling data taken between 1972 and 1981 and is close to the location where *Hudnut et al.* [1989] proposed a series of left-lateral cross faults connecting the southern segment of the San Jacinto fault zone with the Brawley Seismic Zone and southern San Andreas Fault.

There is no clear consensus about how motion on the southern San Andreas makes the transition to the Imperial Fault south of the Salton Sea. One possible model was proposed by *Lomnitz et al.* [1970], who suggested that the spreading centers in the Gulf of California might extend under the continental crust and into the Imperial Valley region (see also *Elders et al.* [1972], *Johnson and Hadley* [1976], *Hill* [1977], *Weaver and Hill* [1978], *Fuis et al.* [1982], *Lachenbruch et al.* [1985], and *Larsen and Reilinger* [1991]). In this scheme, the Brawley Seismic Zone is a spreading center connecting the southern San Andreas to the Imperial Fault. As evidence, *Lomnitz et al.* [1970] noted the existence of several large geothermal fields and recent volcanism in the area, in particular along the southern edge of the Salton Sea near the intrusions at Obsidian Butte, as well as the occurrence of earthquake swarms similar to those observed along oceanic spreading centers. In addition, *Elders et al.* [1972] noted that gravity data from the area show the crust to be significantly thinner southeast of the Salton Sea when compared to the surrounding area, as if it has been stretched in all directions.

A spreading center along the Brawley Seismic Zone could explain some of the dilatational strain rate results seen in Figure 13 since a zone of spreading crust would cause extensional strains in the surrounding area. However, the Brawley Seismic Zone is not oriented northeast-southwest as would be expected for it to connect the southern San Andreas and Imperial fault zones in the traditional stair-step pattern exhibited in oceanic settings. Another possibility is that the spreading is oblique to the Brawley Seismic Zone, combining both right-lateral shear and linear extension perpendicular to the zone, what *Hill* [1977] called a leaky transform fault (see also *Withjack and Jamison* [1986]).

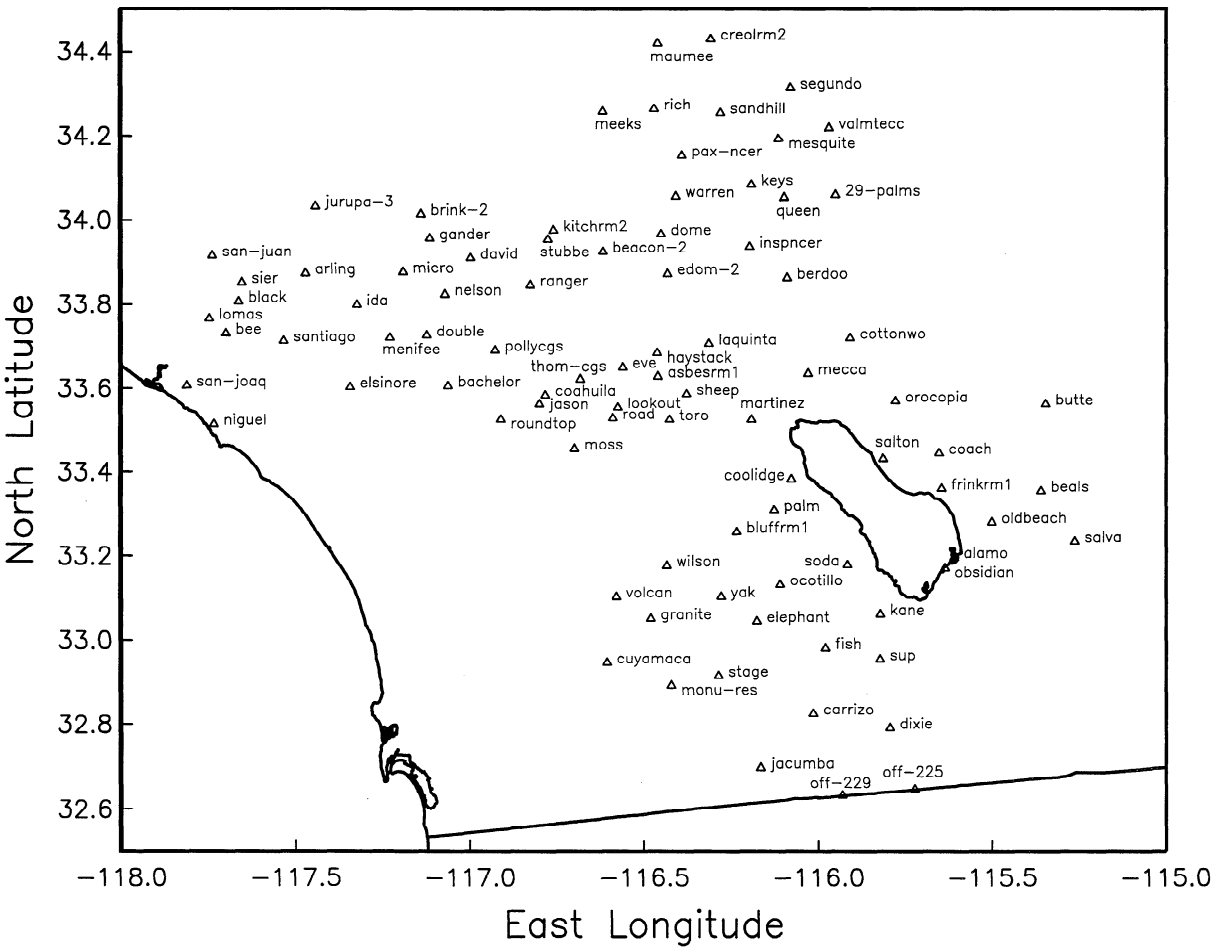

Figure 20. Index map showing the location of Geodolite stations used in this study and referred to in Table 2.

We have modeled this area with each of these two spreading center models: one with a stair-step pattern, the other incorporating oblique spreading. Figures 16a and 16b present a schematic representation of each model along with slip rates and locking depths. These models were used to calculate their effect on all Geodolite stations in Figure 13. The synthetic data resulting from these calculations were then combined into the same four-station subnetworks as with the true Geodolite measurements, and their principal strain rates were calculated. The deformation patterns resulting from each model are shown in Figures 16c and 16d. The modeled deformations look similar to Figure 13, but neither is able to recreate the large zone of dilatation east of the Salton Sea. Each model manages to mimic only one of the seven dilatational observations (highlighted in Figures 16c and 16d). Overall, the oblique spreading center model is much closer to Figure 13 than the stair-step model. In particular, this can be seen in the strain rate results west of the Brawley Seismic Zone. The stair-step model predicts too little north-south contraction and too much east-west extension in this region. Because of this we believe the oblique spreading center model is closer to reality, but even this model does not adequately predict the large zone of dilatational strain rates east of the Salton Sea. Additional geodetic measurements in this area, especially in the part of the Imperial Valley south and east of the Salton Sea where there are no Geodolite stations, would help resolve this dilemma.

Eastern California Shear Zone

Another example of complex deformation is evident in the northern part of the Geodolite network (Figure 17), northeast of Palm Springs. This area is a possible location for motion from the southern San Andreas Fault to be redirected into the Eastern California Shear Zone (ECSZ) of *Dokka and Travis* [1990b] (see also *Sauber et al.* [1986], *Savage et al.* [1990], and *Sauber et al.* [1994]). Additional complications in this area result from the interaction with the active trace of the left-lateral Pinto Mountain Fault.

The strain rate results in Figure 17 due east of Palm Springs show the expected pattern of pure shear with principal axes approximately bisected by the San Andreas Fault. However, as the network continues northward and off the trace of the San Andreas, the strain rate results quickly change to nearly pure east-west extension. This style of deformation continues to the north, with the azimuth of extension slowly rotating to northwest-

southeast, until the network crosses the Pinto Mountain Fault and splits into two lobes, one to the east and one to the northwest. The strain rates in each of these lobes are again essentially pure shear, but the azimuths of these shear signals are consistently different: directed approximately N45°W in the northwestern lobe and N0°W in the eastern lobe.

In their station velocity results, *Lisowski et al.* [1991, Figure 3, p. 8371] show that the stations in the northwestern lobe are moving more slowly with respect to the Pacific Plate than stations in the eastern lobe. They postulated the existence of a northeast trending zone of extension between these two areas to account for the velocity differences. From Figure 17 it would appear that this zone of extension is located along the axis between the two network lobes where northwest-southeast extension predominates.

Figures 18a and 18b present two possible kinematic models for the complex tectonics in this part of the Geodolite network. The elements of the first model (Figure 18a) consist entirely of segments of transcurrent faults; motion of the right-lateral ECSZ simply branches away from the southern San Andreas Fault at a point slightly north of the Salton Sea. The azimuth of the ECSZ was chosen to match the approximate azimuth of the Landers earthquake of June 1992 which ruptured across several faults of the southern Mojave Desert region north of the Pinto Mountain Fault [*Hauksson et al.*, 1993]. The second model (Figure 18b) replaces the short segment of right-lateral fault between the Pinto Mountain and San Andreas with a spreading center similar to the one postulated for the southern Salton Sea area. In this case, however, the azimuth of the spreading center is drawn as being close to perpendicular to both the ECSZ and the San Andreas. In each of these models the position of the triple junction where the ECSZ branches from the southern San Andreas is not stable. In the first model this junction will migrate to the northwest along the San Andreas Fault at 8 mm yr^{-1}, while in the second case the junction migrates in the same direction, but at $8\cos(\alpha)$ mm yr^{-1}, where α is the angle between the spreading center and the San Andreas Fault. For a misalignment of just 7° (i.e., $\alpha = 83°$) the junction will therefore migrate to the northwest at 1 mm yr^{-1}.

The synthetic strain rate results from these two ECSZ models are shown in Figures 18c and 18d. The all-transcurrent faulting model cannot reproduce the zone of linear extension between the San Andreas Fault and the Pinto Mountain Fault. This should not be surprising; only pure shear deformation is produced when a tectonic model consists of transcurrent elements. The spreading center model, however, quite accurately reproduces the observed zone of northwest-southeast extension, as well as the remainder of the strain rate results of Figure 17. The match is not perfect, of course, but it is much closer than the all-transcurrent model, leading us to believe that some form of spreading zone very likely exists at this junction between the San Andreas Fault and the ECSZ.

Each of the models in Figure 18 was intentionally constructed to result in a migrating triple junction where the ECSZ branches from the southern San Andreas Fault, though this result is almost inevitable simply because of the geometry of the faults in the area. We included this feature in order to match the observations of *Dokka and Travis* [1990a] and *Dokka and Travis* [1990b] that the locus of shear deformation in the Mojave Desert region between the Pinto Mountain Fault to the south and the Garlock Fault to the north has systematically shifted from east to west since late Miocene. Because the azimuth of the southern San Andreas Fault is approximately northwest, migration of the ECSZ triple junction along this fault has the effect of shifting the shear zone to the west. *Dokka and Travis* [1990a] show that the ECSZ originally connected with the northwest trending faults in the Death Valley region at approximately 10.6 Ma. If we mentally run either of the models of Figure 18 backward in time, in order for the ECSZ to line up with the Death Valley faults, the geometry of the situation requires that the ECSZ triple junction was located southeast of its present position in Figure 18 and somewhere along the eastern shore of the present-day Salton Sea. This would place the past ECSZ junction at about the same location as the present Brawley Spreading Center discussed in the previous section. It is at least plausible that the ECSZ broke away from the Brawley Spreading Center 10.6 Ma ago and that the resulting triple junction has been migrating northwest along the southern San Andreas Fault since that time.

Finally, we note that the Landers earthquake (June 28, 1992) occurred within and beyond the northernmost part of the Geodolite network we are discussing here. The principal strain rate patterns in this area are oriented at angles of about 45° to the strike of the local faults as would be expected for right-lateral shear strain to accumulate on the Johnson Valley and associated faults which broke in this M_L 7.4 event. There has been speculation that the Pinto Mountain Fault had a controlling influence on the extent of the rupture zone for both the Landers earthquake and the earlier Joshua Tree earthquake (April 23, 1992, M_L 6.1). The mainshock and aftershocks of the Joshua Tree event were almost entirely south of the Pinto Mountain Fault, while the Landers mainshock initiated just north of this fault and continued to rupture to the north [*Hauksson et al.*, 1993]. The dramatic change in character of the strain rate estimates to the south and north of the Pinto Mountain Fault provides evidence that this fault has had an important influence on strain accumulation in the area for at least the last 20 years.

Elsinore Fault Zone

Finally, we observe that the strain rates along the entire length of the Elsinore Fault are relatively small (Figures 13 and 19). This can also be seen in the shear strain rate profile plots (Figures 9-12) where these subnetworks tend to hover at about 0.1 μrad yr^{-1}. In addition, the seismicity along the Elsinore Fault is quite diffuse (Figure 1) and usually extends all the way to the surface. The fact that the seismicity is shallow, combined with the low strain rates, allows us to infer that the interseismic slip rate on the fault must also be very low (using equation (3)). The only exception to this low strain rate can be seen at the far left in Figures 9 and 19 where the deformation in one subnetwork is about 0.3 μrad yr^{-1}. This subnetwork is in an area which was monitored about half as often as the main body of the network, which explains the large error bars. In addition, two of the line length plots between these four stations show a nonlinear accumulation of deformation (as previously mentioned in the data section of this paper). This

nonlinearity is likely due to the fact that one of the stations was destroyed by construction work for a housing project. The eccentric marks were not destroyed, but the resulting ties to reduce the Geodolite data to a common point are suspect (M. Lisowski personal communication, 1991). Whatever the cause, we are suspicious of this single high strain rate result.

Conclusions

The large amount of information contained in Figure 7 (also tabulated in Table 2 and Figure 20) is a tribute to the high quality, and consistency, of the USGS Geodolite program. We believe that the approach taken here, of dividing the data into smaller subnetworks, is a valuable tool to be used for looking at the spatial details of the deformation field. By estimating strain rates instead of station velocities, we have been able to identify several interesting features which were not readily seen in previous studies.

Looking to the future, it is perhaps worth noting that the accuracy attained by these Geodolite distance measurements is roughly comparable to the best of the current GPS systems over the distance range of interest for regional crustal deformation studies (a few kilometers to a few tens of kilometers). As such, the quality of this 18-year span of measurements in the southern California region (and in the many other areas monitored by the USGS throughout the western United States) will not be matched by any of the newer geodetic systems until after the beginning of the twenty-first century.

Acknowledgements. The authors would like to thank Jim Savage, Mike Lisowski, and Will Prescott of the U.S. Geological Survey for providing the raw Geodolite data on which this work is based. In particular, we would like to thank Mike Lisowski for answering all of our questions about details of the data. The text was greatly improved through reviews by Bob King, Roger Bilham, and Lewis Gilbert; we thank the latter in particular for several useful organizational suggestions. This work was supported by the U.S. Geological Survey and the National Science Foundation.

References

Allen, C. R., M. Wyss, J. N. Brune, A. Grantz, and R. E. Wallace, Displacements on the Imperial, Supperstition Hills, and San Andreas Faults triggered by the Borrego Mountain earthquake, *U.S. Geol. Surv. Prof. Pap., 787*, 1972.

Bibby, H. M., The reduction of geodetic survey data for the detection of earth deformation, *Geophys. Div. Rep. 84*, Dep. of Sci. and Ind. Res., Wellington, New Zealand, 1973.

Bibby, H. M., Crustal strain from triangulation in Marlborough, New Zealand, *Tectonophysics, 29*, 529-540, 1975.

Bibby, H. M., Geodetically determined strain across the southern end of the Tonga-Dermadec-Hikurangi subduction zone, *Geophys. J. R. Astron. Soc., 66*, 513-533, 1981.

Bibby, H. M., Unbiased estimate of strain from triangulation data using the method of simultaneous reduction, *Tectonophysics, 82*, 161-174, 1982.

Bilham, R. G., and R. J. Beavan, Strains and tilts on crustal blocks, *Tectonophysics, 52*, 121-138, 1979.

Bird, P., and R. W. Rosenstock, Kinematics of present crust and mantle flow in southern California, *Bull. Seismol. Soc. Am., 95*, 946-957, 1984.

Brunner, F. K., R. Coleman, and B. Hirsch, A comparison of computation methods for crustal strains from geodetic measurements, *Tectonophysics, 71*, 281-298, 1981.

Davis, J. L., W. H. Prescott, J. L. Svarc, and K. J. Wendt, Assessment of global positioning system measurements for studies of crustal deformation, *J. Geophys. Res., 94*, 13635-13650, 1989.

Dokka, R. K., and C. J. Travis, Late Cenozoic strike-slip faulting in the Mojave Desert, California, *Tectonics, 9*, 311-340, 1990a.

Dokka, R. K., and C. J. Travis, Role of the eastern California shear zone in accommodating Pacific-North American plate motion, *Geophys. Res. Lett., 17*, 1323-1326, 1990b.

Elders, W. A., R. W. Rex, T. Meidav, P. T. Robinson, and S. Biehler, Crustal spreading in southern California, *Science, 178*, 15-24, 1972.

Frank, F. C., Deduction of earth strains from survey data, *Bull. Seismol. Soc. Am., 56*, 35-42, 1966.

Fuis, G. S., W. D. Mooney, J. H. Healey, B. A. McMechan, and W. J. Lutter, Crustal structure of the Imperial Valley region, *U.S. Geol. Surv. Prof. Pap., 1254*, 1982.

Happer, J., D. Agnew, Y. Bock, H. Johnson, K. Stark, F. Wyatt, and D. Jackson, Results from continuous GPS measurements over a 14-km line (abstract), *Eos, Trans. AGU, 72*, (44), Fall Meeting suppl., 118, 1991.

Hauksson, E., L. M. Jones, K. Hutton, and D. Eberhart-Phillips, The 1992 Landers earthquake sequence: Seismological observations, *J. Geophys. Res., 98*, 19835-19858, 1993.

Hill, D. P., A model for earthquake swarms, *J. Geophys. Res., 82*, 1347-1352, 1977.

Hudnut, K. W., L. Seeber, and J. Pacheco, Cross-fault triggering in the November 1987 Superstition Hills earthquake sequence, southern California, *Geophys. Res. Lett., 16*, 199-202, 1989.

Jennings, C. W., Fault map of California with locations of volcanos, thermal springs and thermal wells, Williams and Heintz map corporation, Capitol Heights, Md., 1988.

Johnson, C. E., and D. M. Hadley, Tectonic implications of the Brawley earthquake swarm, Imperial Valley, California, January 1975, *Bull. Seismol. Soc. Am., 66*, 1133-1144, 1976.

Johnson, H. O., Techniques and studies in crustal deformation, Ph.D. thesis, Univ. of Cal. San Diego, 1993.

Johnson, H. O., F. K. Wyatt, and D. C. Agnew, Strain accumulation and fault models: An investigation of USGS Geodolite measurements in southern California, paper presented at NSF-USGS Workshop on Crustal Deformation Measurement and Earthquake Mechanics, Morro Bay, Cal., 1990.

King, N. E., and J. C. Savage, Strain-rate profile across the Elsinore, San Jacinto, and San Andreas Faults near Palm Springs, California, 1973-81, *Geophys. Res. Lett., 10*, 55-57, 1983.

Lachenbruch, A. H., J. H. Sass, and S. P. Galanis Jr., Heat flow in southernmost California and the origin of the Salton Trough, *J. Geophys. Res., 90*, 6709-6736, 1985.

Larsen, S., and R. Reilinger, Age constraints for the present fault configuration in the Imperial Valley, California: Evidence for northwestward propagation of the Gulf of California rift system, *J. Geophys. Res., 96*, 10,339-10,346, 1991.

Lisowski, M., J. C. Savage, and W. H. Prescott, The velocity field along the San Andreas Fault in central and southern California, *J. Geophys. Res., 96*, 8369-8389, 1991.

Lomnitz, C., F. Mooser, C. R. Allen, J. N. Brune, and W. Thatcher, Seismicity and tectonics of the northern gulf of California region, Mexico—Preliminary results, *Geofis. Int., 10*, 37-48, 1970.

Margrave, G. F., and E. Nyland, Strain from repeated geodetic surveys by generalized inverse methods, *Can. J. Earth Sci., 17*, 1020-1030, 1980.

Nicholson, C., L. Seeber, P. Williams, and L. R. Sykes, Seismicity and fault kinematics through the Eastern Transverse Ranges, California: Block rotation, strike-slip faulting and low-angle thrusts, *J. Geophys. Res., 91*, 4891-4908, 1986.

Prescott, W. H., An extension of Frank's method for obtaining crustal shear strains from survey data, *Bull. Seismol. Soc. Am., 66*, 1847-1853, 1976.

Press, W. H., B. P. Flannery, S. A. Teukolsky, and W. T. Vetterling, *Numerical Recipes*, Cambridge University Press, New York, 1987.

Reilinger, R., A strain anomaly near the southern end of the San Andreas Fault, Imperial Valley, California, *Geophys. Res. Lett., 12*, 561-564, 1985.

Rockwell, T., C. Loughman, and P. Merifield, Late Quaternary rate of slip along the San Jacinto fault zone near Anza, southern California, *J. Geophys. Res., 95*, 8593-8605, 1990.

Sanders, C. O., and H. Kanamori, A seismotectonic analysis of the Anza seismic gap, San Jacinto fault zone, southern California, *J. Geophys. Res., 89*, 5873-5890, 1984.

Sauber, J., W. Thatcher, and S. C. Solomon, Geodetic measurements of deformation in the central Mojave Desert, California, *J. Geophys. Res., 91*, 12683-12693, 1986.

Sauber, J., W. Thatcher, S. C. Solomon, and M. Lisowski, Geodetic slip rate for the eastern California shear zone and the recurrence time of Mojave Desert earthquakes, *Nature, 367*, 264-266, 1994.

Savage, J. C., Strain accumulation in western United States, *Anu. Rev. Earth Planet. Sci., 11*, 11-43, 1983.

Savage, J. C., and W. H. Prescott, Precision of Geodolite distance measurements for determining fault movements, *J. Geophys. Res., 78*, 6001-6008, 1973.

Savage, J. C., W. H. Prescott, M. Lisowski, and N. King, Deformation across the Salton Trough, California, 1973-1977, *J. Geophys. Res., 84*, 3069-3079, 1979.

Savage, J. C., W. H. Prescott, M. Lisowski, and N. E. King, Strain accumulation in southern California, 1973-1980, *J. Geophys. Res., 86*, 6991-7001, 1981.

Savage, J. C., W. H. Prescott, and G. Gu, Strain accumulation in southern California, 1973-1984, *J. Geophys. Res., 91*, 7455-7473, 1986.

Savage, J. C., M. Lisowski, and W. H. Prescott, An apparent shear zone trending north-northwest across the Mojave Desert into Owens Valley, eastern California, *Geophys. Res. Lett., 17*, 2113-2116, 1990.

Sharp, R. V., Variable rates of late Quaternary strike slip on the San Jacinto fault zone, southern California, *J. Geophys. Res., 86*, 1754-1762, 1981.

Sieh, K. E., and P. L. Williams, Behavior of the southernmost San Andreas Fault during the past 300 years, *J. Geophys. Res., 95*, 6629-6645, 1990.

Snay, R. A., and M. W. Cline, Geodetically derived strain at Shelter Cove, California, *Bull. Seismol. Soc. Am., 70*, 893-901, 1980.

Thatcher, W., Nonlinear strain buildup and the earthquake cycle on the San Andreas Fault, *J. Geophys. Res., 88*, 5893-5902, 1983.

Weaver, C. S., and D. P. Hill, Earthquake swarms and local crustal spreading along major strike-slip faults in California, Pure Appl. Geophys., *117*, 51-64, 1978.

Weldon, R. J. II, and K. E. Sieh, Holocene rate of slip and tentative recurrence interval for large earthquakes on the San Andreas Fault, Cajon Pass, southern California, *Bull. Seismol. Soc. Am., 96*, 793-812, 1985.

Withjack, M. O., and W. R. Jamison, Deformation produced by oblique rifting, *Tectonophysics, 126*, 99-124, 1986.

D. C. Agnew, H. O. Johnson, and F. K. Wyatt, U. C. San Diego, IGPP-0225, 9500 Gilman Drive, La Jolla, CA 92093-0225. (e-mail: hjohnson@ucsd.edu)

(Received September 20, 1993; revised July 18, 1994; accepted July 20, 1994.)